

Solar Wind with Field Lines and Energetic Particles (SOFIE) Model: Application to Historical Solar Energetic Particle Events

Lulu Zhao¹, Igor Sokolov¹, Tamas Gombosi¹, David Lario², Kathryn
Whitman^{3,4}, Zhenguang Huang¹, Gabor Toth¹, Ward Manchester¹, Bart van
der Holst¹, Nishtha Sachdeva¹

¹Department of Climate and Space Sciences and Engineering, University of Michigan, Ann Arbor, MI,
48103, USA

²NASA Goddard Space Flight Center, 8800 Greenbelt Rd, Greenbelt, MD 20771, USA

³University of Houston, 4800 Calhoun Rd, Houston, TX, 77204, USA

⁴KBR, 601 Jefferson Street, Houston, TX, 77002, USA

Key Points:

- Solar Energetic Particles
- Space Radiation Prediction
- Space Weather Forecast

Abstract

In this paper, we demonstrate the applicability of the data-driven and self-consistent solar energetic particle model, Solar-wind with Field-lines and Energetic-particles (SOFIE), to simulate acceleration and transport processes of solar energetic particles. SOFIE model is built upon the Space Weather Modeling Framework (SWMF) developed at the University of Michigan. In SOFIE, the background solar wind plasma in the solar corona and interplanetary space is calculated by the Alfvén Wave Solar-atmosphere Model(-Realtime) (AWSOM-R) driven by the near-real-time hourly updated Global Oscillation Network Group (GONG) solar magnetograms. In the background solar wind, coronal mass ejections (CMEs) are launched by placing an imbalanced magnetic flux rope on top of the parent active region, using the Eruptive Event Generator using Gibson-Low model (EEGGL). The acceleration and transport processes are modeled by the Multiple-Field-Line Advection Model for Particle Acceleration (M-FLAMPA). In this work, nine solar energetic particle events (Solar Heliospheric and INTERplanetary Environment (SHINE) challenge/campaign events) are modeled. The three modules in SOFIE are validated and evaluated by comparing with observations, including the steady-state background solar wind properties, the white-light image of the CME, and the flux of solar energetic protons, at energies of ≥ 10 MeV.

Plain Language Summary

In this paper, we describe one physics-based solar energetic particle model, called Solar-wind with Field-lines and Energetic-particles (SOFIE). This model is designed to simulate the acceleration and transport processes of solar energetic particles in the solar atmosphere and interplanetary space. SOFIE is built on the Space Weather Modeling Framework (SWMF) developed at the University of Michigan. There are three modules in the SOFIE model, the background solar wind module, the coronal mass ejection (CME) initiation and propagation module, and the particle acceleration and transport module. The background solar wind plasma in the solar corona and interplanetary space is modeled by the Alfvén Wave Solar-atmosphere Model(-Realtime) (AWSOM-R) driven by the near-real-time hourly updated Global Oscillation Network Group (GONG) solar magnetograms. In the background solar wind, the CMEs are launched by placing an unbalanced magnetic flux rope on top of the active region, using the Eruptive Event Generator using Gibson-Low configuration (EEGGL). The acceleration and transport pro-

cesses are then modeled self-consistently by the Multiple-Field-Line Advection Model for Particle Acceleration (M-FLAMPA). Using SOFIE, we modeled nine historical solar energetic particle events. The performance of the model and its capability in making space radiation prediction is discussed.

1 Introduction

Solar energetic particles (SEPs) can be accelerated over a wide range of energies extending up to GeVs. They are hazardous not only to humans in space but also to electronics and other sensitive components of spacecraft affecting their operations. Protons of >100 MeV with elevated fluxes exceeding 1 proton flux unit (pfu) are responsible for an increased astronaut exposure inside spacecraft shielding, and protons of >150 MeV are very difficult to shield against as they can penetrate 20 gm cm^{-2} (7.4 cm of Al, or 15.5 cm of water/human tissue) (e.g. Reames, 2013). Furthermore, > 500 MeV protons can penetrate the atmosphere and pose radiation hazards to aviation. Besides protons, energetic heavy ions can also be of severe radiation concerns. Therefore, a reliable prediction of the timing and absolute flux of energetic protons above different energies is needed to provide support for future space exploration. However, the sparsity and large variability of SEP events make them difficult to predict.

Many currently-existing SEP prediction models use post-eruptive observations of solar flares/CMEs to predict SEP events (e.g. Balch, 2008; Smart & Shea, 1976, 1989, 1992; Inceoglu et al., 2018; X. Huang et al., 2012; Belov, 2009; Garcia, 2004; Laurenza et al., 2009; Richardson et al., 2018). There are also models that make predictions of the eruptive events (flares, CMEs, SEPs) using solar magnetic field measurements (Georgoulis, 2008; Park et al., 2018; Bobra & Ilonidis, 2016; Bobra & Couvidat, 2015; X. Huang et al., 2018; Boucheron et al., 2015; Falconer et al., 2014; Bloomfield et al., 2012; Colak & Qahwaji, 2009; Papaioannou et al., 2015; Anastasiadis et al., 2017; Engell et al., 2017; García-Rigo et al., 2016; Tiwari et al., 2015; Kasapis et al., 2022). In addition, because of the shorter transit times of relativistic electrons or very high energy protons compared to ~ 10 MeV protons, near-real-time observations of \sim MeV electrons (Posner, 2007) and/or >100 MeV protons (Boubrabimi et al., 2017; Núñez, 2015; Nunez, 2011) have also been used to predict the arrival of >10 MeV protons.

A recent review by Whitman et al. (2022) summarizes more than three dozen SEP models to predict the occurrence probability and/or properties of SEP events. In Whitman et al. (2022), three approaches of the prediction models are discussed, empirical, machine learning (ML) and physics-based models. Empirical and ML models are built upon potential causality relations between the observable and predictable and they can make rapid predictions, often within seconds or minutes after the input data becoming available. Such models hold value as they can generally issue forecasts prior to the peak of an SEP event. However, since empirical and ML models are built upon historic events, it is difficult to validate their predictions at locations where no routine/historical observations have been made, e.g., the journey from Earth to Mars. And predictions can only be made for the specific energy channels upon which these models are built/trained. These models may also have difficulty in predicting extreme events since there are few such events available for training (e.g. Bain et al., 2021; Núñez, 2015; Whitman et al., 2022). On the other hand, physics-based models are based on first principles (Tenishev et al., 2021; Schwadron et al., 2010; Alberti et al., 2017; Alho et al., 2019; Marsh et al., 2015; Hu et al., 2017; Sokolov et al., 2004; Borovikov et al., 2018; Wijzen et al., 2020, 2022; Li et al., 2021; Luhmann et al., 2007; Aran et al., 2017; Strauss & Fichtner, 2015; Kozarev et al., 2017; Kozarev et al., 2022; Linker et al., 2019; Zhang & Zhao, 2017). Physics-based models are usually computationally expensive, and in order for the physics-based models to make meaningful predictions, they need to run faster than real-time. Moreover, many of the underlying physical mechanisms involved in the development of SEP events are still under-debate, including the particle acceleration processes in the low corona, the particle’s interaction with turbulence magnetic field in the heliosphere, and the seed particles that are injected into the particle acceleration processes. However, physics-based models are still highly attractive, since they solve the acceleration and transport processes of energetic particles and therefore they are able to provide time profiles and energy spectra of SEPs at any location of interest in the heliosphere.

In this work, we demonstrate our attempt to model and make potential predictions of the energetic protons by using the self-consistent physics-based model, called SOLar wind with FIeld lines and Energetic particles (SOFIE). In this paper, we will apply the SOFIE model to nine historical SEP events. These nine SEP events are chosen from the

Solar Heliospheric and INterplanetary Environment (SHINE) challenge/campaign events, which were selected based on their elevated intensities that were relevant to operations¹.

2 SOFIE

In order to build a physics-based SEP model, a background solar wind module, a CME generation and propagation module, and a particle acceleration and transport module are required. In SOFIE, the background solar wind plasma in the solar corona and interplanetary space is modeled by the Alfvén Wave Solar-atmosphere Model(-Realtime) (AWSoM-R) driven by hourly solar magnetograms obtained from the Global Oscillation Network Group (GONG) of the National Solar Observatory (NSO). CMEs are launched by placing an imbalanced magnetic flux rope on top of the parent active region, using the Eruptive Event Generator using Gibson-Low configuration (EEGGL). The acceleration and transport processes of energetic particles are then modeled by the Multiple-Field-Line-Advection Model for Particle Acceleration (M-FLAMPA). All the three modules are fully integrated through the Space Weather Modeling Framework (SWMF) developed at the University of Michigan. In this section, we briefly introduce each module.

2.1 Background Solar Wind

The 3D global solar wind plasma in the Solar Corona ($1 R_s$ - $20 R_s$) and inner heliosphere ($20 R_s$ - 5 AU) is modeled by using AWSoM-R as configured in the SWMF (Sokolov et al., 2013, 2021; Gombosi et al., 2018, 2021). AWSoM-R is an Alfvén wave-driven, self-consistent solar atmosphere model, in which the coronal plasma is heated by the dissipation of two discrete turbulence populations propagating parallel and antiparallel to the magnetic field (Sokolov et al., 2013). The AWSoM-R solar wind model has been validated by comparing simulations and observations of both the in-situ macroscopic properties of the solar wind and the line-of-sight (LoS) appearance of the corona as observed in different wavelengths (Sachdeva et al., 2019; Gombosi et al., 2021). The inner boundary of AWSoM-R is characterized by the magnetic field measurement made by either ground-

¹ <https://ccmc.gsfc.nasa.gov/challenges/sep/shine2018/>, <https://ccmc.gsfc.nasa.gov/challenges/sep/shine2019/>, <https://ccmc.gsfc.nasa.gov/community-workshops/ccmc-sepval-2023/>

based or space-based observatories. In all the SEP events we modeled in this work, hourly-updated GONG solar magnetograms are used.²

A validated background solar wind solution is critical in modeling the transport processes of energetic particles as it provides the magnetic field configuration where particles propagate, allowing the computation of the energetic particle properties observed by spacecraft at specific heliospheric locations. Numerical solutions of the full set of ideal or resistive magnetohydrodynamic (MHD) equations so far have not been able to reproduce aligned interplanetary stream lines and magnetic field lines in corotating frames. One of the reasons for this discrepancy is the numerical reconnection across the heliospheric current sheet: the reconnected field is directed across the current sheet, while the global solar wind streams along the current sheet, thus resulting in “V-shaped” magnetic field lines and significant misalignment between field lines and stream lines. It is impossible to follow particles’ trajectory in “V-shaped” magnetic field lines, therefore, stream lines are usually used instead (Young et al., 2020). Within regular MHD, there is no mechanism to re-establish the streamline-fieldline alignment. Recently, Sokolov et al. (2022) introduced the Stream-Aligned MHD method that “nudges” the magnetic field lines and plasma stream lines towards each other. A detailed explanation and illustration of this method is discussed in Sokolov et al. (2022). In SOFIE, we will solve Stream-Aligned MHD to get a steady state solar wind plasma background representative of the pre-event ambient solar wind and magnetic medium where CMEs and SEPs propagate.

2.2 CME Initiation and Propagation

The CME generation in SOFIE is modeled by the EEGGL module in SWMF (Manchester, Gombosi, Roussev, Zeeuw, et al., 2004; Manchester, Gombosi, Roussev, Ridley, et al., 2004; Manchester et al., 2006; Manchester, van der Holst, & Lavraud, 2014; Manchester, Kozyra, et al., 2014; Lugaz et al., 2005, 2007; Kataoka et al., 2009; Jin et al., 2016; Jin, Manchester, van der Holst, et al., 2017; Shiota & Kataoka, 2016; Borovikov et al., 2017). The initial conditions of the CME within the solar corona is treated by inserting an unstable (or force imbalanced) flux rope suggested by Gibson and Low (1998) into an active region. The magnetogram from GONG and the observed CME speed (from Coordinated Data Analysis Web (CDAW) catalog and/or The Space Weather Database Of

² <https://gong.nso.edu/data/magmap/>

Notifications, Knowledge, Information (DONKI) database) are used to calculate the flux rope parameters. This approach offers a relatively simple, and inexpensive model for CME initiation based on empirical features of pre-event conditions (e.g. Gombosi et al., 2021). The EEGGL module is publicly available for download at <http://csem.engin.umich.edu> or can also be used through the website of the Community Coordinated Modeling Center (CCMC, <https://ccmc.gsfc.nasa.gov/eeggl/>). The subsequent propagation of CMEs in the solar corona and interplanetary medium are modeled using the AWSoM-R module. The EEGGL model to initialize CMEs and the subsequent CME/ICME evolution has been extensively used and validated (e.g. Jin, Manchester, van der Holst, et al., 2017; Manchester & van der Holst, 2017; Manchester, van der Holst, & Lavraud, 2014; Manchester, Gombosi, Roussev, Ridley, et al., 2004; Manchester et al., 2012, 2005, 2008; Manchester, van der Holst, & Lavraud, 2014; Roussev et al., 2004; Roussev, 2008; van der Holst et al., 2009, 2007).

2.3 Particle Tracker

In SOFIE, protons are accelerated at the shocks driven by CMEs through first order Fermi acceleration mechanism (Krymsky, 1977; Axford et al., 1977; Blandford & Ostriker, 1978; Bell, 1978a, 1978b). The acceleration and transport processes are modeled by the M-FLAMPA module in SWMF. In M-FLAMPA, the time-evolving magnetic field lines are extracted from the AWSoM-R solutions, along which the particle distribution functions are solved, following the Parker diffusion equation (Sokolov et al., 2004; Borovikov et al., 2018). Novel mathematical methods are applied to the extracted magnetic field lines to sharpen the shocks thus making the Fermi acceleration process to be more efficient (Sokolov et al., 2004). The injection of suprathermal protons into the CME-driven shock acceleration system is described in Sokolov et al. (2004). The interaction between the energetic protons and turbulent magnetic fields is modeled by the diffusion processes along the background magnetic field lines. The diffusion coefficient close to the shock region is calculated self-consistently through the total Alfvén wave intensities obtained in the MHD simulation, and a Kolmogorov spectrum with an index of $-5/3$ is assumed. The diffusion coefficient upstream of the shock is calculated by assuming a constant mean free path. Detailed parameter settings will be discussed in Section 4.

3 Overview of the Nine SEP Events

The nine SHINE challenge events were primarily chosen because they were large SEP events that were relevant to operations. Specifically, the 2012 July 12 event was selected because there was a large particle enhancement at Mars. In this section, we describe the observational facts of the nine SEP events. Table 1 summarizes the observational facts of the CMEs and solar flares associated with the solar origin of the nine events. From left to right, each column shows the SEP event date used to identify the event, the associated CME onset time, the CME speed, the soft X-ray flare class and onset time, the NOAA active region locations on the Sun, and the NOAA active region (AR) number. The CME onset time is estimated from observations made by the Large Angle and Spectrometric Coronagraph (LASCO) instrument on board Solar & Heliospheric Observatory (SOHO). Note that all the CMEs associated with the SEP events modeled in this work are categorized as halo CME in the SOHO LASCO CME catalog CDAW³. Each individual SEP event has been studied extensively by many papers as described below. Key features of each individual event are as follows:

2012-Mar-07 Event: The solar origin of this SEP event is temporally associated with a X5.4 class X-ray from the NOAA Active Region (AR) 11429 at N17E15. At 00:24 UT, a fast halo CME with a plane-of-sky speed of 2040 km s⁻¹ was detected in LASCO/C2 coronagraph images. At 01:05 UT, a second flare with a class of X1.3 erupted from the same active region and a slower halo CME with a speed of 1825 km s⁻¹ was detected. Detailed analyses of these two eruptions can be found elsewhere (e.g. Patsourakos et al., 2016). The fact that the first CME was faster than the second CME and that the electron intensities measured by the MErcury Surface, Space ENvironment, GEochemistry, and Ranging (MESSENGER) at 0.31 AU peaked before the occurrence of the second flare (c.f. Figure 6 in Lario et al., 2013) suggest that the main contributor to the observed SEP event was the first solar eruption. In fact, in the analysis of SEP events observed by the two spacecraft of the Solar Terrestrial Relations Observatory (i.e., Solar TERrestrial RELations Observatory (STEREO)-Ahead and STEREO-Behind) and near-Earth spacecraft, Richardson et al. (2014) and Kouloumvakos et al. (2016) concluded that the first flare/CME was responsible for the SEP event at all three locations. Therefore, in the simulation, we will consider only the first CME. Yet the energetic particle measure-

³ https://cdaw.gsfc.nasa.gov/CME_list/halo/halo.html

Table 1. Observational facts of the nine SEP events

Event Date	CME Onset Time ^a [UT]	CME Speed ^b [km/s]	SXR GOES Flare Class/Onset [UT]	NOAA AR
2012-Mar-07	2012-Mar-07 00:24	2040	X5.4/00:02	N17E15(11429)
2012-May-17	2012-May-17 01:37	1263	M5.1/01:25	N12W89(11476)
2012-Jul-12	2012-Jul-12 16:54	1400	X1.4/15:37	S14W02(11520)
2013-Apr-11	2013-Apr-11 07:24	743	M6.5/06:55	N09E12(11719)
2014-Jan-07	2014-Jan-07 18:12	2048	X1.2/18:04	S15W11(11943)
2017-Jul-14	2017-Jul-14 01:25	750	M2.4/01:07	S09W33(12665)
2017-Sep-04	2017-Sep-04 20:24	1323	M5.5/20:12 ^c	S08W16(12673)
2017-Sep-06	2017-Sep-06 12:12	1816	X9.3/11:53	S08W34(12673)
2017-Sep-10	2017-Sep-10 15:48	2087	X8.2/15:35	S08W88(12673)

^a The onset time is obtained from the SHINE challenge websites and visually examined. to match the SOHO observations.

^bThe CME speed is provided by the SHINE challenge website.

^cBased on inspection of SDO/AIA images.

ment made by Geostationary Operational Environmental Satellite (GOES) shows two clear onset phases, which may correspond to the two CMEs. The peak and decay phases of the intensity profile was indistinguishable.

2012-May-17 Event: This event was the first Ground Level Enhancement (GLE) of solar cycle 24 with >433 MeV proton intensity enhancements detected by GOES-13 and up to $\gtrsim 7$ GeV as inferred from neutron monitor observations (Balabin et al., 2013; Li et al., 2013). This GLE, designated as GLE71, had the peculiarity of having a highly anisotropic onset as detected by several neutron monitor stations (Mishev et al., 2014). By assuming that relativistic protons propagated scatter-free along nominal interplanetary field lines, Li et al. (2013) estimated that ~ 1.12 GeV protons were released at about 01:39 \pm 00:02 UT, in accordance with a type II radio burst and prominence eruption at the origin of the associated fast CME, and corresponding to a height of the CME at $\sim 3.07 R_s$. It is worth noting that Shen et al. (2013) reported two CME eruptions from the same active region that were separated by about 2 minutes. However, in the time intensity profiles of energetic protons detected by GOES, the two eruptions were not well separated. In this work, we will only consider the first CME eruption as the main accelerators of energetic particles. The same approach was adopted by Li et al. (2021) who modeled this event using AWSoM and improved Particle Acceleration and Transport in the Heliosphere model (iPATH) models.

2012-Jul-12 Event: The CME at the origin of this SEP event generated the fourth strongest geomagnetic storm of solar cycle 24 (Gil et al., 2020). The prompt component of this SEP event showed >100 MeV proton intensity enhancements as observed by GOES-13 (c.f. Figure 6 in Gil et al., 2020) and the arrival of the shock at 1 AU driven by the CME was accompanied by a strong energetic storm particle (ESP) event (e.g. Wijzen et al., 2022). Details of the solar eruption that generated this event, reconstructions of the CME structure as observed by coronagraphs, and the topology of the CME at its arrival at 1 AU can be found in Scolini et al. (2019), Gil et al. (2020) and references therein.

2013-Apr-11 Event: This SEP event was the first Fe-rich event of solar cycle 24 as evidenced by ion data collected by STEREO-B and near-Earth spacecraft (Cohen et al., 2014). The filament eruption origin of the CME that generated this SEP event has been studied by several authors (e.g. Vemareddy & Mishra, 2015; Joshi et al., 2017; Fulara et al., 2019). The EUV wave associated with the origin of this event propagated mostly

toward the footpoint of the nominal interplanetary magnetic field line connecting to STEREO-B, but signatures of the EUV wave reaching the footpoints of the interplanetary magnetic field lines connecting to either STEREO-A or near-Earth spacecraft were not observed (Lario et al., 2014). The non-arrival of the EUV wave at the magnetic footpoint of a given spacecraft does not preclude the observation of SEPs by such a spacecraft. Lario et al. (2013) concluded that observation of particles by near-Earth spacecraft was due to the CME-driven shock expanding at higher altitudes over a wide range of longitudes, without leaving an observable EUV trace in the low corona, being able to accelerate and inject particles onto the field lines connecting to near-Earth locations.

2014-Jan-07 Event: The solar eruption at the origin of the CME associated with the SEP event was analyzed in detail by Möstl et al. (2015). They showed that the CME was “channeled” by strong nearby active region magnetic fields and open coronal fields into a non-radial propagation direction within $\sim 2.1 R_S$, in contrast to deflection in interplanetary space. This phenomenon will be discussed in more detailed in Section 4, where a white-light coronagraph comparison between the simulation and observation is discussed. Mays et al. (2015) studied the propagation of this CME up to 1 AU and determined that only a glancing CME arrival was observed at Earth. The SEP intensity enhancement occurred on the tail of a very energetic SEP event with onset on 2014 January 6 (see details in, e.g., Thakur et al., 2014; Köhl et al., 2015).

2017-Jul-14 Event: The origin of this event was associated with a medium-sized (M2.4) long-duration (almost two hours) flare from a large active region that displayed a sigmoidal configuration associated with a filament/flux rope. A high-lying coronal EUV loop was seen moving outward, which was immediately followed by the impulsive phase of the flare (Jing et al., 2021). The formation of the sigmoidal filament/flux rope, its expansion, and the evolution of the photospheric magnetic field, leading to the eruption of the filament and the resulting CME have been studied in detail by James et al. (2020) (see their Figure 13). The arrival of the shock at Earth, accompanied by local particle intensity increases at energies $\lesssim 10$ MeV, generated a geomagnetic storm $K_p=6$.

2017-Sep-04 Event: This SEP event, together with the following two SEP events, are a series of SEP events that occurred in early September 2017, towards the end of solar cycle 24. The solar eruptions associated with the origin of these events and their geomagnetic effects were analyzed by Chertok et al. (2018) and Shen et al. (2018) and ref-

erences therein, whereas the resulting SEP events were described by Bruno et al. (2019) among others. The flare associated with the first SEP event occurred at 20:12 UT on 2017 Sep 4 and the CME occurred at 20:24 UT with a speed of 1323 km s^{-1} . The active region (AR 12673) was located at S09W16. The flare onsets time was estimated from the SDO/AIA movies. From SOHO/LASCO C2 images, around two hours before the eruption of the CME associated with the SEP event, there was a preceding CME at 18:48 UT on 2017 Sep 4 with a speed of 597 km s^{-1} (CDAW). From the point of view of SOHO/LASCO, the first CME propagates to the west whereas the second faster CME propagates toward the southwest. The second CME overtook the previous CME shortly after its eruption, around 21:24 UT. In this work, we attribute the main acceleration of protons to the second CME, which is faster and stronger.

2017-Sep-06 Event: A X9.3 class flare occurred at 11:54 UT on 2017 Sep 6 from the same active region AR 12673 as the 2017-Sep-04 event. At this time, the active region was located at S08W34. The CME has a speed of 1816 km s^{-1} . The occurrence of this SEP event was in the decay phase of the previous event, making the identification of the onset of the energetic proton intensity enhancements at different energies difficult.

2017-Sep-10 Event: At 15:35 UT on 2017 Sep 10, the same active region AR 12673 produced a X8.2 class flare. The active region rotated to S08W88. The corresponding CME has a speed of 2087 km s^{-1} . This event is an GLE event, GLE #72. This event was also well-studied by multiple groups (see details in Ding et al., 2020; Zhu et al., 2021).

4 SOFIE Results

In this section, we present the results of the SOFIE model in simulating the nine SEP events. When modeling each event, we first run the AWSoM-R model to get a steady state solution of the background solar wind. In doing so, the hourly GONG magnetogram measured right before the flare eruption is chosen to drive the AWSoM-R model. The simulation domain extends from 1.105 solar radius (R_s) to 2.5 AU. In Section 4.1, we discuss the background solar wind solutions for each event and compare them with in-situ observations made by near-Earth instruments. After getting the steady state solar wind solution, an imbalanced magnetic flux rope is placed on top of the active region where the CME erupted from. In Section 4.2, we show the 3D topology of the magnetic flux rope and compare the white-light coronagraph images calculated from simulation

with the LASCO/C2 observations. In Section 4.3, we show the 2D spatial distribution of energetic particles in a sphere around Earth and the extracted proton flux time profiles.

4.1 Background Solar Wind

The highly dynamic solar wind background and the complex geometry of the coronal magnetic field can vary significantly in each Carrington rotation and from event to event. Therefore, instead of using a homogeneous background solar wind for each event, we calculate the background solar wind properties individually. The plasma properties at Earth’s location is extracted from the 3D MHD solution and compared with the in-situ measurement made by spacecraft. As shown in Figure 1, the macroscopic properties of the background solar wind for the nine SEP events are shown. For each event, a total time period of 27 days is shown, corresponding approximately to the synodic solar rotation period. In this paper, we only show the in-situ properties of the solar wind and its validation against the observation. The validation of the AWSoM(-R) model using the predicted line-of-sight (LoS) appearance of the corona in different wavelengths has been discussed in detail in Sachdeva et al. (2019) and Gombosi et al. (2021).

In each panel of Figure 1, the solar wind properties including the radial bulk plasma speed (U_r), the proton number density (N_p), the temperature, and the total magnetic field magnitude (B) are plotted from top to bottom. The simulation results are plotted in red and the observations, measured by the Advanced Composition Explorer, are plotted in black. The time period corresponding to the passage of the ICME are plotted in shaded teal. The ICME time periods are obtained from the list of ICMEs observed at 1 AU⁴ (Cane & Richardson, 2003; Richardson & Cane, 2010). Since we solve the steady state background solar wind, the ICME structures, which are the counterparts of the CMEs in interplanetary space, are not modeled and will not be compared. Most of the SEP events occur in solar maximum, especially the ones that we model in this work. Therefore, in multiple panels of Figure 1, one can see more than one ICMEs in the observations. As we mentioned above, the ICMEs in the observations will not be captured by the simulation. The mismatch between the simulation and observation in the ICME time period

⁴ <https://izw1.caltech.edu/ACE/ASC/DATA/level3/icmetable2.htm>

is as expected. Except the ICMEs, the overall dynamics of the solar wind plasma are well-represented by the simulation.

When running the AWSoM-R model, to get a reasonable comparison between the simulations and observations, there are two adjustable input parameters: the Poynting flux parameter and the correlation length of the Alfvén wave dissipation (see details in Z. Huang et al., 2023; van der Holst et al., 2014; Jivani et al., 2023). The Poynting flux parameter determines the input energy at the inner boundary to heat the solar corona and accelerate the solar wind, and the correlation length describes the dissipation of Alfvén wave turbulence in the solar corona and heliosphere (Z. Huang et al., 2023). When running the AWSoM-R model to obtain the background solar wind, we varied the Poynting Flux parameter to get the best comparison between the simulations and observations. A detailed discussion on choosing the optimal Poynting flux parameter is discussed in detail in a recent paper by Z. Huang et al. (2023).

4.2 CMEs

After obtaining the steady state background solar wind solution, we then launch the CME from the location of the parent active region by placing an imbalanced Gibson-Low (Gibson & Low, 1998) magnetic flux rope. The parameters of the flux rope, including the total magnetic field, the flux rope size, and the flux rope orientation, are calculated based on the GONG magnetogram and the observed CME speed. In Figures 2, 3, and 4, we show the 3D topology of the inserted flux rope (left column), the white-light image measured by the LASCO/C2 telescope (middle column), and the synthetic white-light image calculated from the simulation (right column). In the left column, the surface of the Sun (at 1.105 Rs) and a number of 3D magnetic field lines are colored according to the radial component of the magnetic field. Note that the Sun and the magnetic field lines do not share the same color bar. The color bar shown in each plot represents the magnetic field strength on the magnetic field lines. The radial magnetic field on the Sun (at 1.105 Rs) ranges from -20 Gauss to 20 Gauss. The large scale magnetic field lines, besides the flux rope, are plotted to represent the overall structures of the coronal magnetic fields in each event. It is clearly seen that the field configurations differ dramatically from event to event. And the overall magnetic field strength on the solar surface also varies orders of magnitude. The perspective view of the Sun is that obtained from Earth. Therefore, due to the projection effect, the flux rope of some events are not

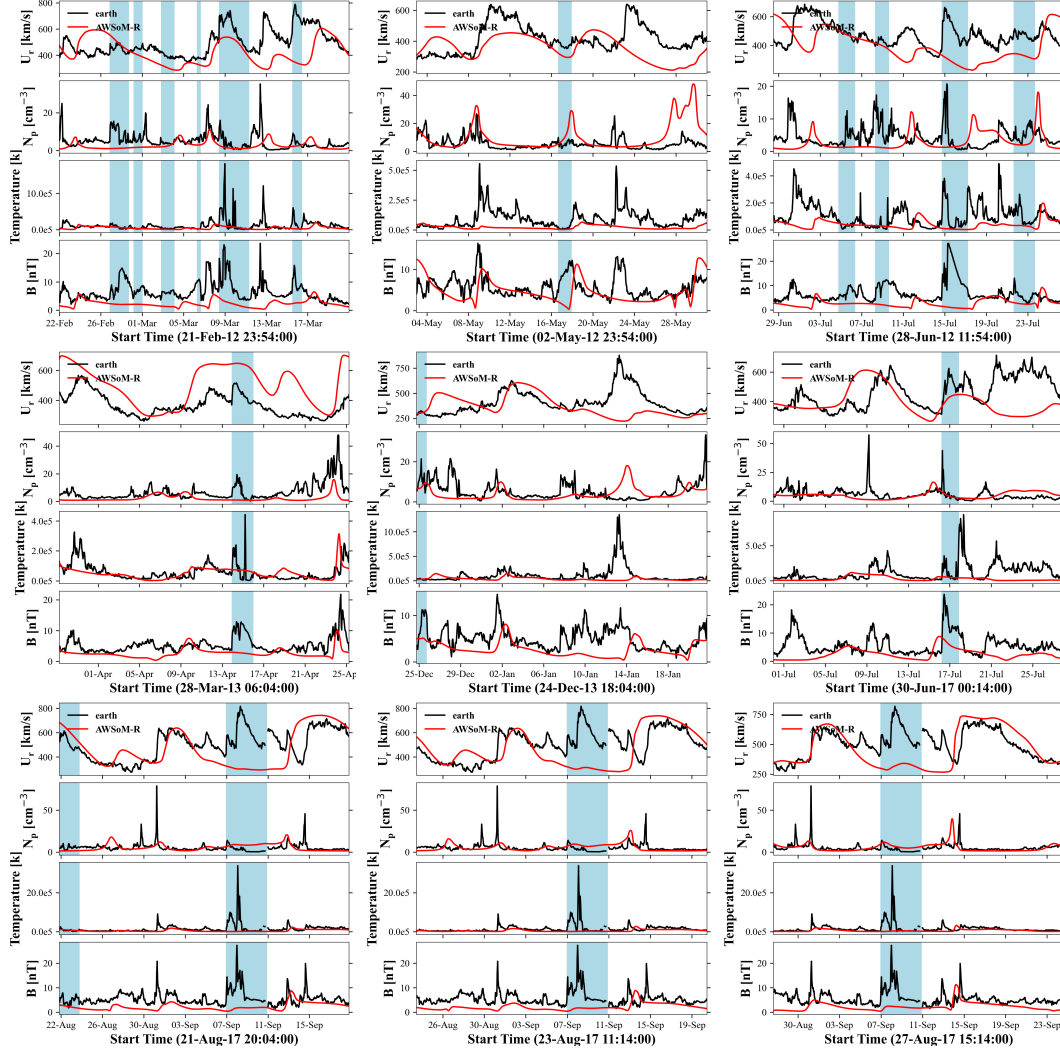


Figure 1. Macroscopic properties of the background solar wind for the nine SEP events. In each panel, the radial solar wind plasma speed, the solar wind density, the temperature and the magnitude of the total magnetic field is shown from the top to bottom respectively. The simulation results from AWSoM-R are plotted in red and observations are plotted in black. The passage of the ICME structures are shaded in teal.

as distinguishable as the others, especially when the flux rope is located close to the center of the Sun, as viewed from Earth.

The middle and right columns of Figures 2, 3, and 4 compare the white-light coronagraph observations (middle) and simulations (right) several tens of minutes after the eruption of each CME. The exact times shown in Figures 2, 3, and 4 are selected on the basis of their clear CME detection in the LASCO/C2 field of view. The exact time of the selected observational frame is shown in the title of each image. The images calculated from the simulation are chosen accordingly and the time, dt , after the CME eruption is shown.

In the following, we briefly describe the white-light comparison of each individual CME between the observation and simulation. In the 2012-Mar-07 event (top row of Figure 2), the core structure of the CME compares well, and the leading edge of the CME reaches approximately the same radial distance between observation and simulation, although the overall expansion of the CME in the simulation is narrower than the observation, especially in the left flank. In the 2012-May-17 event (middle row of Figure 2), the core structure, the leading edge, and the overall expansion of the CME are well-captured by the simulation. In the 2012-Jul-12 event (bottom row of Figure 2), the CME is a halo CME (CDAW) and the flux rope originated from the center of the Sun as seen from Earth (left column). Therefore, the projection effect is large. From the LASCO/C2 image (middle column), the core structure of the CME has a southern part (the active region is located at S14W02), which is captured in the simulation.

In the 2013-Apr-11 event (top row of Figure 3), the core structure of the CME propagates toward the east as seen in the LASCO/C2 images. The envelope of the CME appears to be symmetric with respect to the solar equator. However, in the white-light image obtained from the simulation, the northern part of the CME is brighter than the southern part, demonstrating an extreme asymmetric shape. We examined the plasma properties in the low solar corona and found a high density region lying in front of the flux rope which slowed down the propagation of the CME and led to such an asymmetric structure.

In the 2014-Jan-07 event (middle row of Figure 3), the CME erupted from the active region located at S15W11. From the LASCO/C2 point of view, the CME was a halo CME but propagating mostly in the southwest direction. The initial simulation also ob-

415 tains a halo (not shown here), which does not have the southwestern part as seen from
 416 the LASCO/C2 images. Therefore, it is very likely that the CME was deflected towards
 417 the west in the very early stage. We examined the magnetic fields around the active re-
 418 gion where the flux rope was inserted and found there was a strong active region in the
 419 east of the flux rope. The CME eruption and propagation in this event has been ana-
 420 lyzed in detail by Möstl et al. (2015). They found the CME was “channeled” by strong
 421 nearby active region magnetic fields and open coronal fields into anon-radial propaga-
 422 tion direction within $\sim 2.1 R_s$. In the current setup of simulations, since the initial speed
 423 of the CME was 2048 km s^{-1} , the flux rope is difficult to be deflected in the early stage.
 424 Therefore, in order to match that of the LASCO/C2 observation and also match the sub-
 425 sequent propagation of the CME, we shifted the location of the flux rope to the adja-
 426 cent active region in the west, separated by 8° in longitude from the active region listed
 427 in Table 1. As seen from Figure 3, the simulated CME propagates toward southwest-
 428 ern, which is comparable to the observations. However, the shifting of the flux rope to
 429 the west leads to issues when modeling the particle acceleration and propagation.

430 In the 2017-Jul-14 event (bottom row of Figure 3), the white-light image from the
 431 observation and simulation is comparable, except that the CME shows a bright north-
 432 ern part in the simulation. While in the observation, the core part of the CME leans to-
 433 ward the south. The 2017-Sep-04 event (top row of Figure 4) involved two CMEs. From
 434 the LASCO/C2 movie, there was a preceding CME eruption that occurred around 2 hours
 435 before the main CME, with a speed of 597 km s^{-1} (CDAW). The previous CME prop-
 436 agated toward the west and the main CME took over the previous CME shortly after
 437 the eruption. In the LASCO/C2 image (top row of Figure 4), we enclose the leading edge
 438 of the main CME for a better vision comparison with the simulation. In the simulation,
 439 we only launch the main CME. The radial distance of the CME leading edge and its prop-
 440 agation direction is in a good agreement with the observation. Both the 2017-Sep-06 and
 441 2017-Sep-10 events (middle and bottom rows of Figure 4) show very good agreement be-
 442 tween simulations and observations, in terms of the CME speed and propagation direc-
 443 tion, including the interaction of the flux rope with the high density streamers in the back-
 444 ground solar wind.

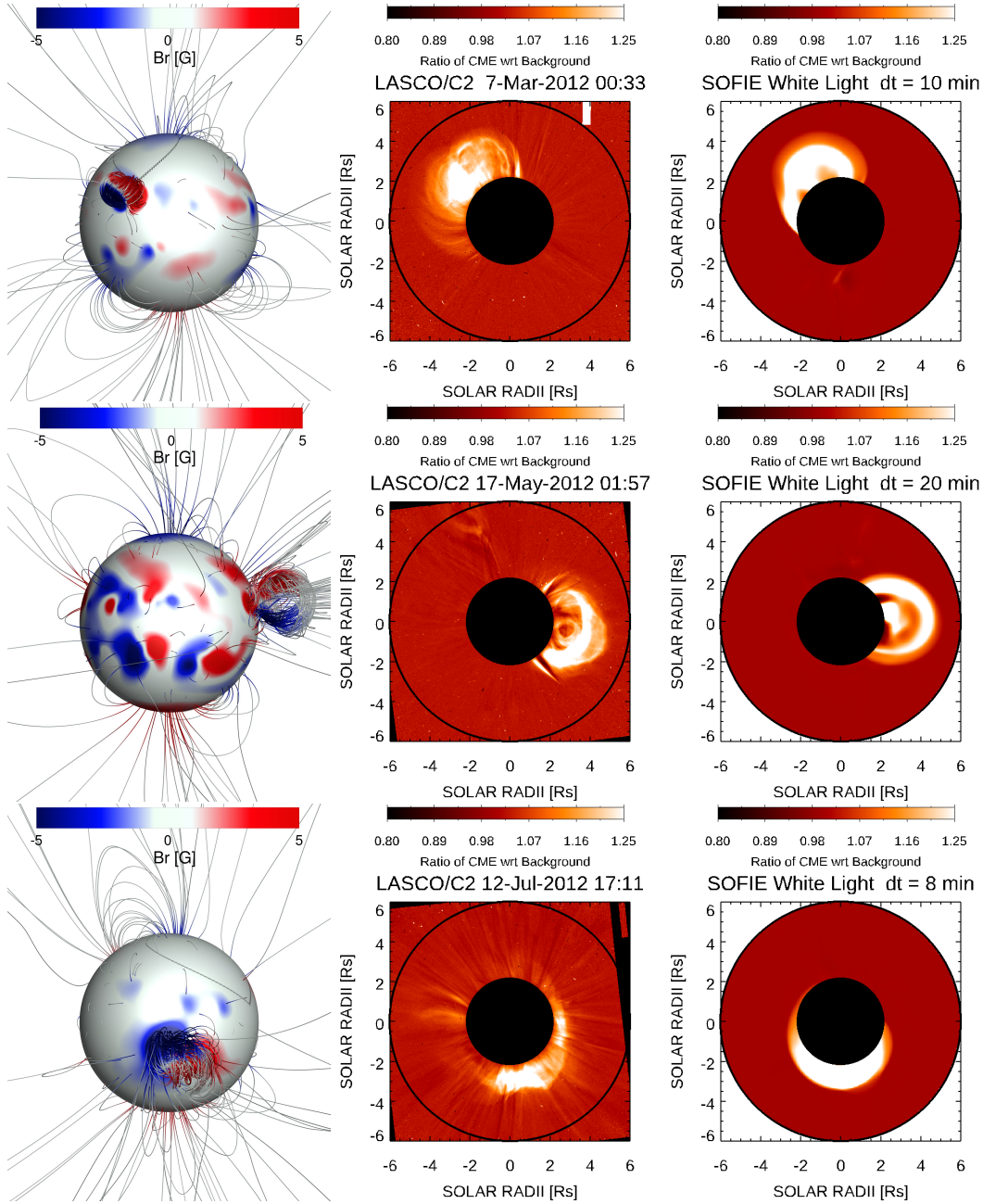


Figure 2. Left: The 3D topology of the inserted magnetic flux rope in the active region. Middle: LASCO/C2 white-light image of the solar corona. Right: White-light image calculated from the simulation at the same time as the middle column. Three events are shown here, 2012-Mar-07, 2012-May-17, and 2012-Jul-12. In the left column, the surface of the Sun (1.105 Rs) and the 3D magnetic field lines are colored with the radial magnetic field. The color bar shown in the plot presents the strength of the radial magnetic field in the field lines. The radial magnetic field on the Sun ranges from -20 Gauss to 20 Gauss (color bar not shown here).

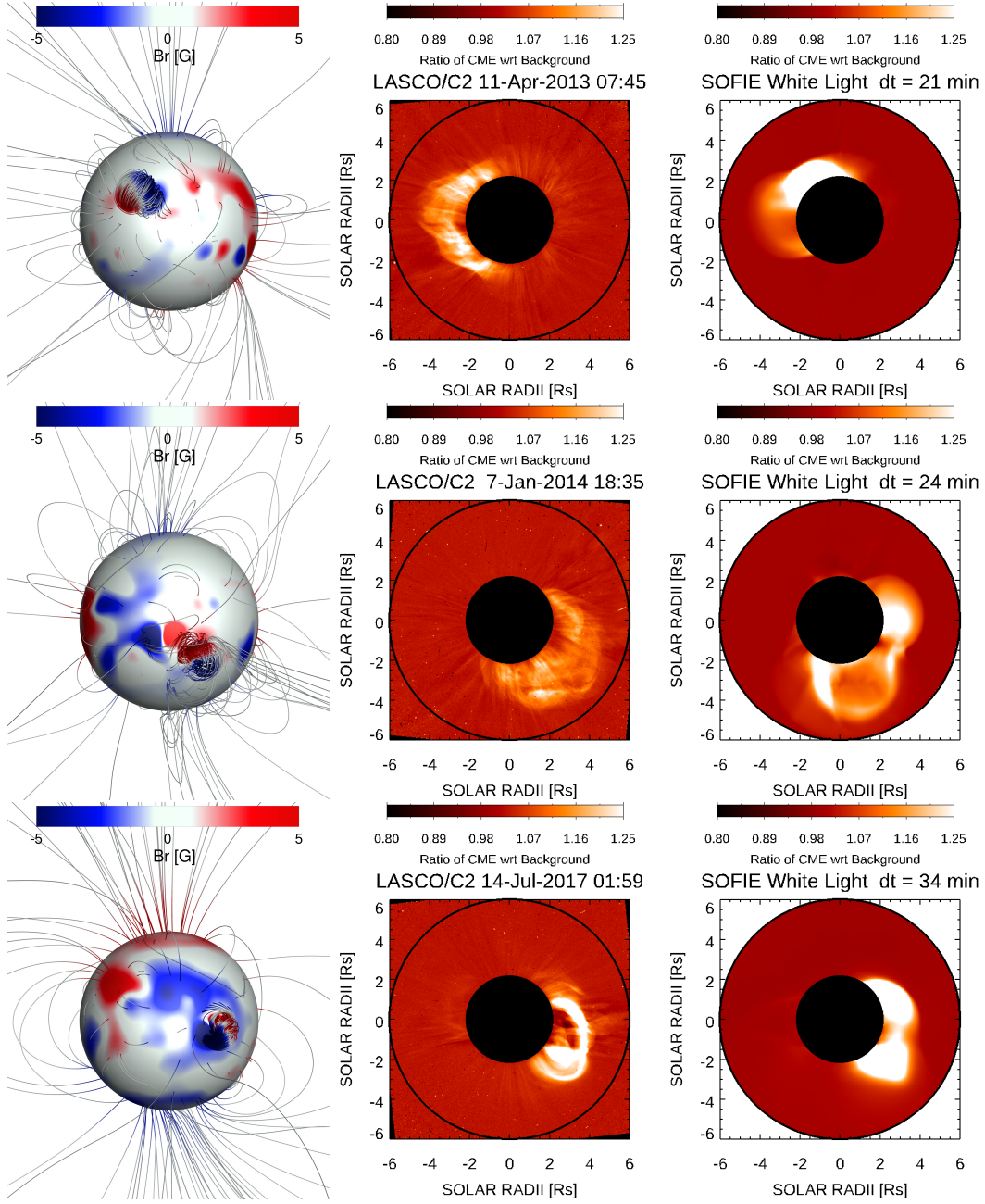


Figure 3. In the same format as Figure 2 for the three events 2013-Apr-11, 2014-Jan-07, and 2017-Jul-14.

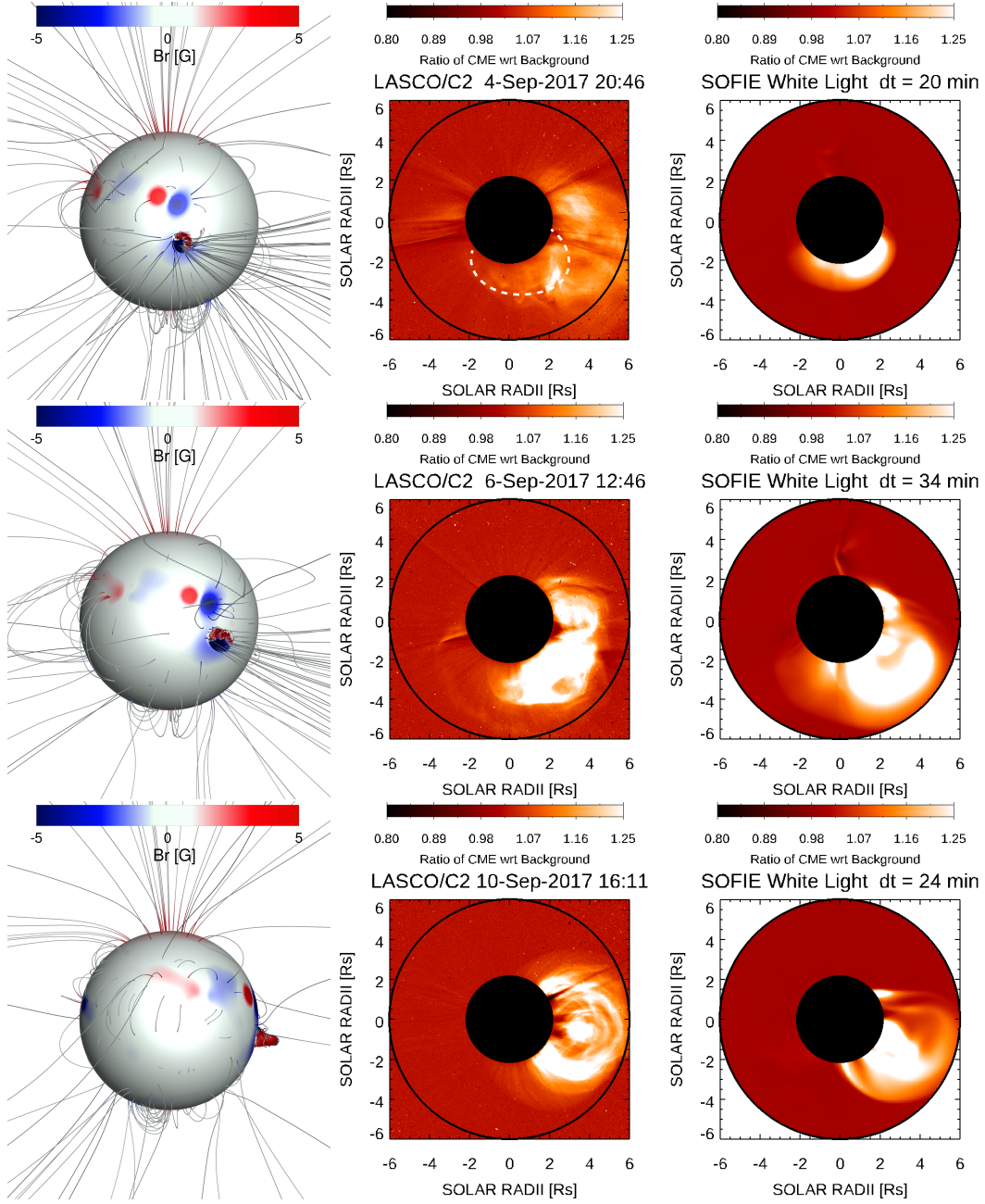


Figure 4. In the same format as Figure 2 for the three events 2017-Sep-04, 2017-Sep-06, and 2017-Sep-10.

4.3 Energetic Particles

Once the force-imbalanced flux rope was inserted into the active region, we run the coupled AWSoM-R and M-FLAMPA modules to solve the energetic particle acceleration and transport processes in the solar corona and inner heliosphere. More than 600 magnetic field lines are extracted from the 3D AWSoM-R solution. The extracted magnetic field lines are followed in the local Lagrangian reference frame convecting with the solar wind plasma. A frequent (120 s) dynamic coupling between AWSoM-R and M-FLAMPA is performed to account for the propagation of the CME and CME-driven shock wave. In the simulation, the shock is identified by the sudden jump of the solar wind velocity along the extracted magnetic field lines. On each individual magnetic field line, the Parker diffusion equation is solved in the time-evolving Lagrangian coordinates. The diffusion strength close to the shock is determined by the total Alfvén wave intensity calculated self-consistently from the AWSoM-R simulation. The diffusion mean free path upstream of the shock, as described in Sokolov et al. (2004), is assumed to be a constant value, 0.3 AU. This setup is for simplicity and in the future simulations, the diffusion coefficients in the entire domain will be calculated from the AWSoM-R solution. In this set of runs, perpendicular diffusion due to the field line random walk is not modeled. In modeling the nine SEP events, we followed 648 magnetic field lines that cover 360° in longitude and -45° to 45° in latitude of the solar surface. The starting radial distance of the magnetic field lines is $2.5 R_s$, and the magnetic field lines are traced inward and outward until reaching the inner and outer boundaries. The starting points of the magnetic field lines are chosen to distribute uniformly in the sphere enclosed $2.5 R_s$. The latitudes of the active region that we insert the flux rope are within $\pm 17^\circ$ around the solar equator. Therefore, a $\pm 45^\circ$ coverage in latitudes is sufficient to calculate the particle flux in the ecliptic plane.

In this work, we are not trying to solve the injection problem, instead, we set the injection energy, E_i , in the shock system to be 10 keV. The absolute level of the injected particles is determined by assuming a suprathermal tail ($\sim p^{-5}$) extending from the thermal momentum ($\sqrt{2mT}$) to the injected momentum (p_i) as follows (Sokolov et al., 2004):

$$f(p_i) = \frac{c_i}{2\pi} \frac{n}{(2mT)^{3/2}} \left(\frac{\sqrt{2mT}}{p_i} \right)^5 \quad (1)$$

where m is the proton mass, n and T are the local plasma density and temperature in energy units (if in Kelvins, $k_B T$ should stand instead, k_B being the Boltzmann constant)

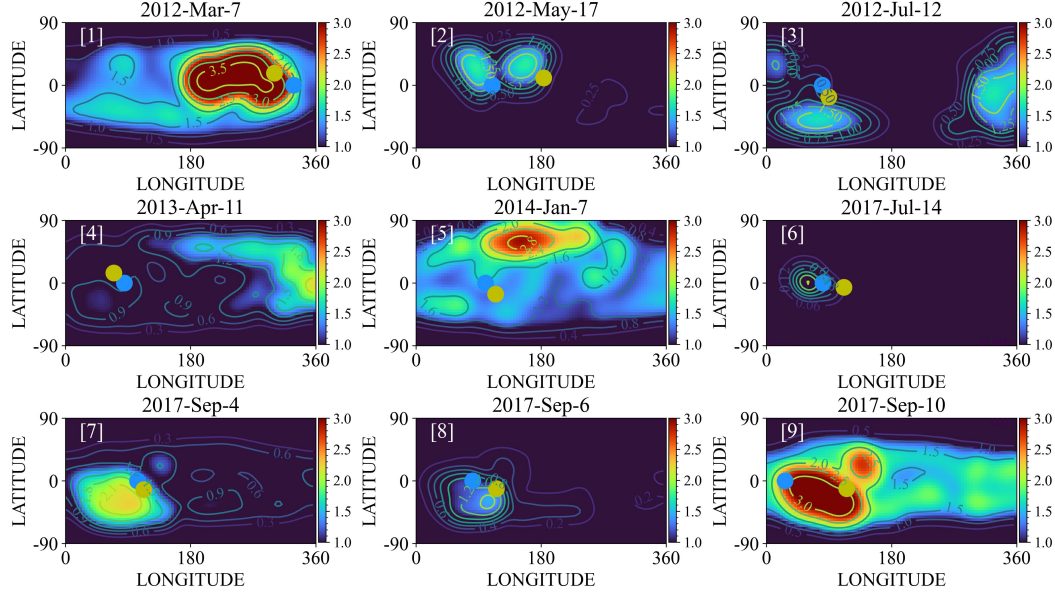


Figure 5. 2D distribution of energetic proton flux at energies greater than 10 MeV. The proton flux is plotted in the logarithm scale. The nine events are plotted in the row-wise order. The x and y axis shows the Carrington longitude and latitude on the sphere at 1 AU. The locations of Earth are marked with blue solid circle, and the location of the inserted flux rope on the Sun are marked with yellow solid circle.

calculated from AWSoM-R simulation. $c_i < 1$ is the injection coefficient and p_i is the injection momentum. The physical meaning of the injection coefficient may be derived by integrating the assumed distribution of the suprathermal particles over momentum, which gives us their density: $4\pi \int_{\sqrt{2mT}}^{p_i} f p^2 dp = c_i n$. Hence, c_i is a fraction of density of protons having suprathermal energy. In order to compare with the observations, the injection level c_i is adjusted for each individual SEP event. These suprathermal particles are then accelerated on the magnetic field lines with negative velocity divergence ($\nabla \cdot \mathbf{u} < 0$). The strength of the acceleration is fully dependent on the jump of plasma velocity, i.e. the shock strength (Sokolov et al., 2004).

4.4 2D Distribution of Proton Flux

Figure 5 shows the 2D distribution of the logarithm of the energetic proton flux 1 hour after the eruption of the CME flux rope, at energies greater than 10 MeV. The x and y axis shows the Carrington longitude and latitude for a sphere at 1 AU. Earth

location is marked with a blue solid circle, and the location of the inserted flux rope on the Sun is marked with a yellow solid circle. The locations of the flux rope are marked in the plot to show the relative locations of Earth with respect to the CME, i.e. the source of energetic particles. Since the interplanetary magnetic fields follow Parker spiral in general (e.g. Zhao et al., 2019), the flux of energetic particles is distributed around $45^\circ \sim 65^\circ$ eastern of the flux rope location, depending on the corona and interplanetary magnetic field configurations. In this set of runs, the injection coefficients are assumed to be uniform across the shock front (shock obliquity independent). Therefore, the 2D distribution of the energetic particles reflects the collective effect of the strength of the shock, the ambient plasma density and the temperature of the flux rope.

In the 2012-Mar-07 event, the parent CME erupted from the active region located at N17E15 (see Table 1), 15 degree eastern of the Earth's longitude. The 2D proton flux distribution in Figure 5 shows maxima around 90 degree eastern of the Earth's location, which is consistent with the overall topology of the interplanetary magnetic fields. In the 2012-May-17 event, the parent CME erupted from the west limb, around 90 degree western of the Earth's longitude. There are two local maxima in the 2D distribution of proton flux, which may be due to the non-uniform strength of the shock driven in front of the propagating flux rope that affects the acceleration process, or the variations of the ambient plasma properties that determines the suprathermal injection.

In the 2012-Jul-12 event, the parent CME erupted from near central meridian as seen from Earth. Since propagation direction of the CME leans toward the south, the proton flux in the southern hemisphere was also elevated due to the southern portion of the flux rope. In the 2013-Apr-11 event, the parent CME erupted from active region located 12 degree eastern of Earth, which is consistent with the 2D distribution of proton flux shown in Figure 5. As we discussed in Section 4.2, the northern part of the CME is brighter than the southern part in the white-light image of the simulation, due to the high density region in front of the flux rope. Such an asymmetry structure was reflected in the 2D distribution plot of proton flux. The proton flux was elevated in the northern hemisphere and extended to a broader region than in the southern hemisphere, corresponding to a stronger particle source in the north.

In the 2014-Jan-07 event, the CME erupted from the active region located at S15W11. However, the 2D proton flux distribution shows local maxima far away from the expected

region. This is due to the fine-tuning process that we performed in matching the white-light images between the observations and simulations as discussed in Section 4.2. The flux rope was inserted to an active region to the west separated by 8 degrees in longitude from the active region that was responsible for the eruption. Meanwhile, the flux rope was also rotated in order to match the simulation with the observations, which leads to the unexpected northward propagation of flux rope. In the 2017-Jul-14 event, the parent CME erupted from S09W33, consistent with the 2D distribution of proton flux. Note that in panel [6] of Figure 5, Earth is very close to the center of the distribution.

The 2017-Sep-04, 2017-Sep-06, and 2017-Sep-10 are a sequence of events that their parent CMEs erupted from the same active region located at 16, 34, and 88 degrees western of the Earth's longitude. As shown in the panels [7], [8], and [9] of Figure 5, the Earth's location was on the western, close to the center, and eastern of the energetic proton source.

The 2D distribution of the energetic proton flux highly depends on the shock properties, i.e. shock strength, along the connected magnetic field lines with the corresponding CME. Furthermore, the absolute particle flux is determined by the number of seed particles that are injected into the shock system. In plotting the 2D distributions shown in Figure 5, we varied the injection coefficient for each individual event in order to obtain comparable results with the observations made by GOES satellite. The relative injection ratio is summarized in Table 2 and will be discussed in detail below. Note that for some events, the injection coefficient is much larger than 1, e.g. the 2012-Mar-07 event and 2014-Jan-07 event. There are many reasons that could lead to such large injection coefficients. One of the reasons is the underestimation of the pre-existing seed particle sources at the event eruption, including the preceding CMEs and the flares. Another factor that will affect the injection coefficient is the combined effect of the magnetic connectivity between the CME shock front and the earth's location with neglecting the perpendicular diffusion in the calculation. A small displacement of the earth's magnetic footpoint with respect to the shock front, together with an overestimation/underestimation of the CME shock properties will lead to a large variation of the proton flux. In this work, the perpendicular diffusion is not modeled, therefore, the proton flux contribution from cross-field diffusion, which is very important for poorly-connected events, is missing.

Table 2. Injection Coefficients of the nine SEP events

Event	Injection Coefficient (c_i)
2012-Mar-07	5
2012-May-17	0.025
2012-Jul-12	0.025
2013-Apr-11	1.25
2014-Jan-07	2.5
2017-Jul-14	0.00025
2017-Sep-04	0.25
2017-Sep-06	0.025
2017-Sep-10	1.25

4.5 Time Profiles

Figure 6 compares proton intensities measured by GOES with the time dependent flux profiles obtained from the simulations. The flux profiles are calculated by extracting the > 10 MeV proton flux at Earth’s location from series of 2D particle distributions as shown in Figure 5. A total of 20 hours are plotted. The horizontal dashed lines represent the 10 particle flux unit (pfu) threshold used by agencies to determine whether the radiation caused by the energetic protons raises any concern. The four vertical dashed lines indicate the times 1h, 5h, 10h, and 15h after the eruption of the CME flux rope. As we mentioned above, the absolute proton flux is multiplied by a factor of the injection coefficient in order to get comparable match between observations and simulations. Therefore, in the following discussion, we focus on the rising phase and relative level of the flux profiles.

Based on the relative location of Earth with respect to the source of energetic protons, a prompt onset of protons is expected for the events when Earth is well-connected to the source of energetic protons. While the proton flux is expected to show a gradual increase if Earth’s location falls outside of the particle source. As shown in the 2D distribution of energetic protons (Figure 5), in most of these events, Earth’s location is on the edge of the particle distribution at 1 AU, including the 2012-Mar-07, 2012-May-17, 2017-Jul-14, 2017-Sep-04, 2017-Sep-06, and 2017-Sep-10 events. In the 2012-Jul-12, 2013-

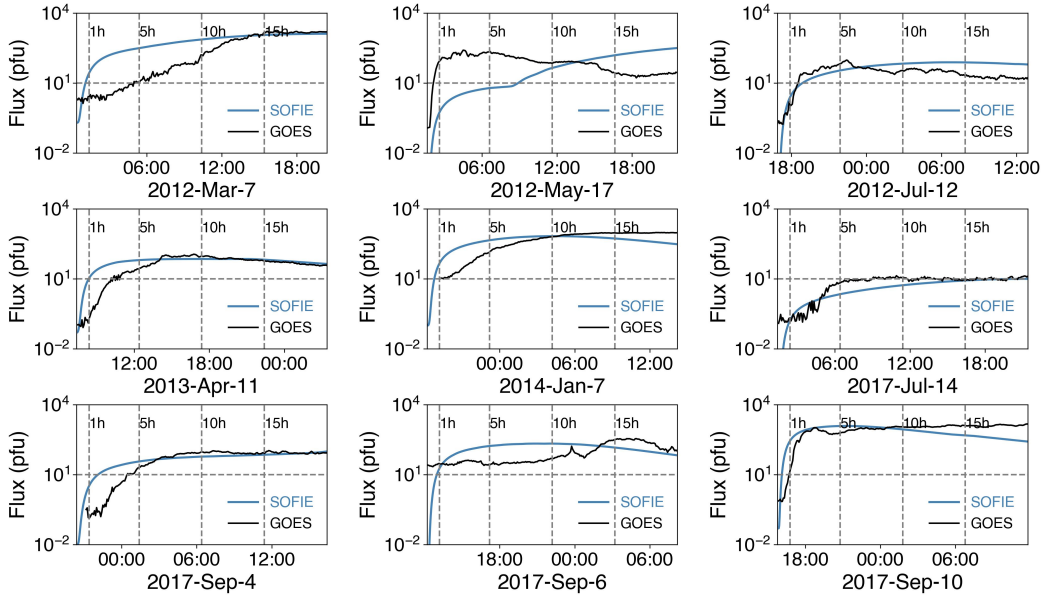


Figure 6. The comparison of proton flux at energies greater than 10 MeV between observations (black) and simulation (blue). Nine events are plotted in the row-wise order. The horizontal dashed line represents the threshold of 10 pfu and the four vertical dashed lines represent 1h, 5h, 10h, and 15h after the CME eruption. A total time period of 20 hours after the CME eruption is shown.

571 Apr-11, and 2014-Jan-07 events, Earth location is far away from the particle distribu-
 572 tion at 1 AU. The change of the proton flux with time, especially in the early phase, de-
 573 pends on the time evolution of the CME flux rope, together with the change of magnetic
 574 connectivity between Earth and the CME.

575 The comparison between the simulations and observations shown in Figure 6 dis-
 576 plays some discrepancies. A number of factors could contribute to these discrepancies.
 577 One of them is the background solar wind medium where the CME flux rope and en-
 578 ergetic protons propagate. The solar wind background in this work is a steady-state so-
 579 lution driven by the solar magnetic fields measured at a single time (before the flare erup-
 580 tion) and the 3D solar wind solution has been compared to measurements obtained from
 581 a single near-Earth point in space that might not be representative of all the medium
 582 sampled by the particles as they propagate from the CME shock front to Earth. And
 583 the solar wind disturbances, including ICMEs, which are abundant during solar max-
 584 imum, are not modeled. A second factor is due to the fact that the longitudinal extent
 585 of the shock may be underestimated/overestimated. Our CME flux-rope white-light sim-
 586 ulation images have been validated with plane-of-sky images of the LASCO/C2 obser-
 587 vation that do not include the extent of the CME in longitude. A third factor is the as-
 588 sumption of the same constant parallel mean free path in all SEP events and the lack
 589 of cross-field diffusion processes when modeling energetic particle transport in interplan-
 590 etary space. Keeping these factors in mind, we discuss the comparisons between simu-
 591 lations and observations for all the events in details below.

592 In the 2012-Mar-07 event, the proton flux calculated from the simulation shows a
 593 prompt increase, which is different from the gradual increase in the observation. This
 594 may due to the CME-driven is narrower in the observation than in the simulation. The
 595 injection coefficient is estimated to be 5. As discussed in Section 3, there are two CME
 596 eruptions associated with this event, and the energetic particles from these two eruptions
 597 merged together after the two clear onset phases. Therefore, the injection coefficient, 5
 598 for this event, may reflect the contribution of the two eruptions. Besides, the > 10 MeV
 599 proton flux was already elevated before the onset of this event from the observations. The
 600 pre-event elevated proton flux is due to a CME eruption that occurred on 2012 Mar 4
 601 at 11:00:07 UT (CDAW).

In the 2012-May-17 event, the onset phase time matches well between the observation and simulation. The second enhancement of proton flux at around 7 hours after the CME eruption was due to the CME evolution and the fact that Earth's magnetic connectivity changed establishing connection with a region with larger proton flux. Due to the second enhancement of the proton flux, the injection coefficient for this event does not reflect the difference of the overall level of proton flux between simulation and observation.

In the 2012-Jul-12 event, the timing of proton flux in the simulation matches very well with the observations, especially in the early phase. The mismatch of the declining of the proton flux after 10 hours may due to the assumption of the mean free path in the simulation. The effect of the mean free path on the decay phase of the proton flux will be discussed below.

In the 2013-Apr-11 event, the calculated proton flux shows a quicker onset phase than the observations. The slower onset may due to the poor magnetic connection of Earth to the CME (with an AR of N09E12). The proton flux after 6 hours between observation and simulation matches quite well and the injection coefficient of 1.25 is a reasonable value.

The 2014-Jan-07 is a special case, as we discussed above. The 2D proton flux distribution shows the particle source is far away from the expected region, due to the fine-tuning processes of the inserted flux rope. Moreover, the > 10 MeV proton flux in the observation was well-above the background due to a previous eruption that occurred at 08:00 UT on 2014 January 06.

The gradual onset phase in the 2017-Jul-14 event matches well between observation and simulation. The injection coefficient in this event is estimated to be $2.5 \cdot 10^{-4}$. This small value of injection could be due to the slower speed of the parent CME, 750 km s^{-1} . However, the CME speed in the 2013-Apr-11 event is 743 km s^{-1} , comparable to the one in the 2017-Jul-14 event, but the 2013-Apr-11 event has an injection coefficient of 1.25. Another reason for the small injection coefficient is that the eruption of the 2017-Jul-14 event was near solar minimum, when the solar activity was low, and the remnant population of prior SEP events that could act as seed particle population for the processes of particle acceleration at the shock could also be low.

The 2017-Sep-04, 2017-Sep-06, and 2017-Sep-10 are a series of events that their parent CMEs erupted from the same active region. The injection coefficients in these three events are 0.25, 0.025, and 1.25. The CMEs associated with the 2017-Sep-04 event are twin-CMEs (Li et al., 2012) as we discussed in Section 3 and shown in Figure 4. The more efficient acceleration in the twin-CME system (Li et al., 2012; Zhao & Li, 2014; Ding et al., 2013) could be one of the potential reasons why the injection coefficient in this event is much larger than the 2017-Jul-14 event, although this event occurred under solar minimum conditions. The 2017-Sep-06 event occurred in the decay phase of the 2017-Sep-04 event. Therefore, the onset phase between the observation and simulation does not compare well. The onset phase in the 2017-Sep-10 event calculated from the simulation is faster than the observation. This may due to the overall extension of the CME flux rope and the magnetic connectivity at the beginning of the event. Similar to the 2012-Jul-12 event, the declining phase in the simulation is faster than the simulation, indicating a faster deceleration of the CME in the simulations or a larger mean free path assumption.

The determination of the injection coefficient in each individual event is affected by the properties of the shocks driven by the eruption of the CME flux rope, including the spatial extension of the shock surfaces and the strengths of the shocks. Hence, the value of the injection coefficient does not necessarily imply there are more or less suprathermal protons, in the energy of 10 keV, that are accelerated in the diffusive shock acceleration process. An estimation of a larger CME flux rope or a stronger CME-driven shock will lead to a smaller injection coefficient and vice versa. Besides, the magnetic connectivity between the Earth's location and the CME shock front also affect the injection coefficient. If the Earth's location is close to the edge of the particle source, a small change of the size of the CME flux rope or a little error in the magnetic connectivity calculation will result in a larger or smaller injection coefficient. From Figures 2, 3, and 4, the comparison between the simulation and observation is only performed for the SOHO observations, which include a large projection effect. In the future work, a multi-spacecraft validation of the white-light CME image will be included. Moreover, together with C2 observation, C3 observation will also be used to monitor the acceleration or deceleration of the CME flux rope in the solar corona. This is because the onset phase contains competing processes between the continuous acceleration of protons and the diffusion process. A significant deceleration of the CME flux rope propagation in the very early phase

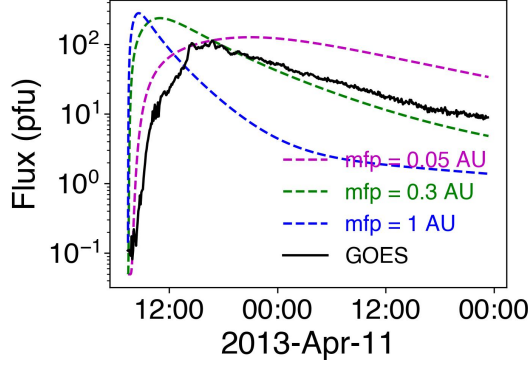


Figure 7. The effect of far-upstream mean free paths on the calculated proton flux profiles in the 2013-Apr-11 event. The GOES observation is plotted in black. The calculated proton flux profiles with different mean paths (mfp) are plotted in magenta (mfp=0.05 AU), green (mfp=0.3 AU), and blue (mfp=1 AU).

would reduce the acceleration efficiency of energetic protons, especially in the larger energy end.

4.6 Decay Phase

The ambient solar wind plasma properties affect the transport of energetic particles, including the magnetic field turbulence. The timing of the first arriving particles, the timing when the particle crosses the preset threshold, (Wang & Qin, 2015; Qin et al., 2006) e.g. 10 pfu, and the time dependent and event-integrated energy spectra (Zhao et al., 2016, 2017) are all impacted by the magnetic field turbulence. In the simulation, the ambient solar wind plasma is calculated by running the steady-state MHD simulation using Stream-Aligned AWSoM-R module in SWMF. The mean free path upstream of the shock is assumed to be 0.3 AU in all of the nine simulations, for simplicity. In Figure 7, we show the effect of different mean free paths on the proton flux profiles for the 2013-Apr-11 event as an example. The magenta, green, and blue dashed curves show the flux profiles with far-upstream mean free paths of 0.05 AU, 0.3 AU, and 1 AU. The calculated proton fluxes are extracted from a sample magnetic field line. Both the onset phase and the decay phases depend on the value of mean free paths in the three cases as expected. Employing the turbulence strength calculated from the MHD simulation is one of the future steps to improve the SOFIE model.

5 Discussion

In this paper, we describe the physics-based SEP model, SOFIE, and its application in modeling nine historical SEP events. The simulations of the SEP events start from calculating the background solar wind using the AWSoM-R model, in which the solution of the solar wind plasma is driven by the measurement of the Sun's magnetic field. The acceleration of energetic protons in SOFIE is solved in the CME-driven shock generated by the eruption of CME flux rope. The CME is modeled by inserting an imbalanced flux rope on the corresponding active region on the Sun using the EEGGL model. The acceleration and transport of energetic protons are modeled using the M-FLAMPA model, in which the Parker diffusion equations are solved along individual time-evolving magnetic field lines. In such regards, SOFIE model is a data-driven and self-consistent SEP model.

In this work, we perform a systematic test of using SOFIE model to simulate SEP events. The steady-state background solar wind macroscopic properties (radial solar wind speed, number density, temperature, total magnetic field strength) calculated from the AWSoM-R is compared and validated against in-situ measurements. The white-light coronagraph image of the erupted flux rope generated by the CME generator, EEGGL, is compared and evaluated with SOHO/LASCO/C2 observations. This is only a single-observer comparison, therefore, the longitudinal extent of the flux rope has not been compared to observations. The proton flux at energies greater than 10 MeV calculated by M-FLAMPA is compared with GOES observation for the first 20 hours. In order to obtain a comparable flux level with observations, different injection coefficients are used for each event. The potential factors that may affect the injection coefficient include the multiple CME eruptions in one SEP event, the elevated suprathermal particles from previous eruptions, and solar activity level. We also discussed the effect of the upstream mean free path on proton flux profiles, especially the declining phase. In the current set of runs, the upstream mean free paths are assumed to be the same for all the events for simplicity. This assumption may lead to a faster or slower declining profile in the simulation. The mean free paths may also affect the onset phase of the SEP event, making it more difficult to evaluate the acceleration/deceleration of CME propagation in the early stage.

The most time and resources consuming part of the SOFIE model is when modeling the propagation of the CME flux rope in the solar corona domain ($1.05 R_s$ to 20

R_s). In this stage, the SOFIE model runs at the same speed as real-time with 2000 cpu cores. It can run faster than real-time if more cpu cores are used. When the CME flux rope leaves the solar corona domain, several hours after the CME eruption, SOFIE model runs much faster than real-time, thus empowering the capability of using SOFIE model in predicting the properties of SEP events.

The necessity of transporting energetic particles in the solar wind solution calculated from an MHD simulation is due to the complex physical processes therein. The transport of energetic particles in interplanetary space involves many different physical processes, including adiabatic cooling, magnetic focusing, as well as parallel and perpendicular diffusion. All these processes depend on the properties of ambient solar wind background. The magnetic field turbulence affects the timing of the first arriving particles, the timing when the particle flux crosses a pre-set threshold (Wang & Qin, 2015; Qin et al., 2006), and the time-dependent and event-integrated energy spectral index (Zhao et al., 2016, 2017). In the set of runs in this work, the upstream mean free paths are assumed to be constant and the effect of magnetic turbulence strength from the AWSoM-R simulation will be discussed in subsequent papers.

Besides the steady-state background solar wind, CMEs and ICMEs, which are the main accelerators of energetic particles travel through the ambient solar wind medium, interact with its surrounding plasma and magnetic field, causing significant distortions and disruptions of the solar wind plasma (Manchester, Gombosi, Roussev, Zeeuw, et al., 2004; Manchester, Gombosi, Roussev, Ridley, et al., 2004; Manchester et al., 2005; Manchester et al., 2008; Manchester et al., 2012). These distortions affect the acceleration and transport of energetic particles. There are also SEP events that are associated with more than one CME eruption, e.g the 2012-Mar-07 and 2017-Sep-04 events. The underlying acceleration of energetic particles is likely to be enhanced according to the twin-CME scenario (Li et al., 2012; Zhao & Li, 2014; Ding et al., 2013). In this work, when modeling the nine historical SEP events, each event is only associated with one CME eruption and the simulation of the background medium does not include prior CMEs that could affect the transport of SEPs. In future work, we will examine the performance of SOFIE in modeling more than one CME eruption.

Open Research Section

The in-situ solar wind plasma properties used in this work is available in the Space Physics Data Facility <https://spdf.gsfc.nasa.gov/>. The white-light image data is available in the SOHO/LASCO website <https://lasco-www.nrl.navy.mil/index.php?p=content/retrieve/products>. The GOES data is available at <https://www.ngdc.noaa.gov/stp/satellite/goes/index.html>. All the simulation data including the 3D steady-state solution of the solar wind plasma, the 2D white-light image data, the 2D distribution of protons, and the time dependent flux profiles are publicly available at the Deep Blue Data Repository maintained by the University of Michigan https://deepblue.lib.umich.edu/data/concern/data_sets/cn69m504s.

Acknowledgments

This work was supported in part by NASA LWS Strategic Capabilities (SCEPTER) project at the University of Michigan under NASA grant 80NSSC22K0892, NASA SWxC grant 80NSSC23M0191 (CLEAR), NASA LWS grant 80NSSC21K0417, NASA R2O2R grant 80NSSC22K0269, NASA HSR grant 80NSSC23K0091, NSF ANSWERS grant GEO-2149771. D.L. acknowledges support also from NASA Living With a Star (LWS) program NNH19ZDA001N-LWS, and the Heliophysics Innovation Fund (HIF) program of the Goddard Space Flight Center. We thank the ACE SWEPAM instrument team and the ACE Science Center for providing the ACE data. We thank the SOHO project, an international cooperation between ESA and NASA. We thank the GOES team. This work utilizes data from the National Solar Observatory Integrated Synoptic Program, which is operated by the Association of Universities for Research in Astronomy, under a cooperative agreement with the National Science Foundation and with additional financial support from the National Oceanic and Atmospheric Administration, the National Aeronautics and Space Administration, and the United States Air Force. The GONG network of instruments is hosted by the Big Bear Solar Observatory, High Altitude Observatory, Learmonth Solar Observatory, Udaipur Solar Observatory, Instituto de Astrofísica de Canarias, and Cerro Tololo Interamerican Observatory. Resources supporting this work were provided, in part, by the NASA High-End Computing (HEC) Program through the NASA Advanced Supercomputing (NAS) Division at Ames Research Center. The authors acknowledge the Texas Advanced Computing Center (TACC) at The University of Texas at Austin for provid-

ing HPC resources that have contributed to the research results reported within this paper. <http://www.tacc.utexas.edu>

References

- Alberti, T., Laurenza, M., Cliver, E. W., Storini, M., Consolini, G., & Lepreti, F. (2017). Solar Activity from 2006 to 2014 and Short-term Forecasts of Solar Proton Events Using the ESPERTA Model. *The Astrophysical Journal*, *838*(1), 59.
- Alho, M., Wedlund, C. S., Nilsson, H., Kallio, E., Jarvinen, R., & Pulkkinen, T. (2019). Hybrid modeling of cometary plasma environments. *Astronomy & Astrophysics*, *630*, A45. Retrieved from <https://doi.org/10.1051/0004-6361/201834863> doi: 10.1051/0004-6361/201834863
- Anastasiadis, A., Papaioannou, A., Sandberg, I., Georgoulis, M., Tziotziou, K., Kouloumvakos, A., & Jiggins, P. (2017). Predicting Flares and Solar Energetic Particle Events: The FORSPEF Tool. *Solar Physics*, *292*(9).
- Aran, A., Pacheco, D., Agueda, N., & Sanahuja, B. (2017). Updating SOLPENCO2 and New Analysis on Downstream FLuence (SOL2UP) Project. *Final Report, ESA/ESTEC Contract 4000114116/15/NL/HK*, 1-90.
- Axford, W. I., Leer, E., & Skadron, G. (1977). The acceleration of cosmic rays by shock waves. *International Cosmic Ray Conference*, *11*, 132.
- Bain, H. M., Steenburgh, R. A., Onsager, T. G., & Stitely, E. M. (2021, July). A summary of national oceanic and atmospheric administration space weather prediction center proton event forecast performance and skill. *Space Weather*, *19*(7), e02670. doi: 10.1029/2020sw002670
- Balabin, Y. V., Germanenko, A. V., Vashenyuk, E. V., & Gvozdevsky, B. B. (2013, January). The First GLE of New 24th Solar Cycle. In *International cosmic ray conference* (Vol. 33, p. 1467).
- Balch, C. C. (2008). Updated verification of the space weather prediction center's solar energetic particle prediction model. *Space Weather*, *6*(1), 1–13.
- Bell, A. R. (1978a, January). The acceleration of cosmic rays in shock fronts. I. *MNRAS*, *182*, 147-156. doi: 10.1093/mnras/182.2.147
- Bell, A. R. (1978b, February). The acceleration of cosmic rays in shock fronts. II. *MNRAS*, *182*, 443-455. doi: 10.1093/mnras/182.3.443

- 809 Belov, A. (2009). Properties of solar X-ray flares and proton event forecasting. *Ad-*
 810 *vances in Space Research*, 43(4), 467–473.
- 811 Blandford, R. D., & Ostriker, J. P. (1978, April). Particle Acceleration by Astro-
 812 physical Shocks. *Astrophys. J. Lett.*, 221, L29-L32. doi: 10.1086/182658
- 813 Bloomfield, D. S., Higgins, P. A., McAteer, R. T., & Gallagher, P. T. (2012). To-
 814 ward reliable benchmarking of solar flare forecasting methods. *The Astrophysi-*
 815 *cal Journal Letter*, 747(2).
- 816 Bobra, M. G., & Couvidat, S. (2015). Solar flare prediction using SDO/HMI vec-
 817 tor magnetic field data with a machine-learning algorithm. *The Astrophysical*
 818 *Journal*, 798(2).
- 819 Bobra, M. G., & Ilonidis, S. (2016). Predicting Coronal Mass Ejections Using Ma-
 820 chine Learning Methods. *The Astrophysical Journal*, 821(2), 1–7.
- 821 Borovikov, D., Sokolov, I. V., Manchester, W. B., Jin, M., & Gombosi, T. I. (2017).
 822 Eruptive event generator based on the Gibson-Low magnetic configuration.
 823 *Journal of Geophysical Research*, 122(8), 7979–7984.
- 824 Borovikov, D., Sokolov, I. V., Roussev, I. I., Taktakishvili, A., & Gombosi, T. I.
 825 (2018). Toward a Quantitative Model for Simulation and Forecast of Solar En-
 826 ergetic Particle Production during Gradual Events. I. Magnetohydrodynamic
 827 Background Coupled to the SEP Model. *The Astrophysical Journal*, 864(1),
 828 88.
- 829 Boubrahimi, S. F., Aydin, B., Martens, P., & Angryk, R. (2017). On the prediction
 830 of >100 MeV solar energetic particle events using GOES satellite data. *IEEE*
 831 *International Conference on Big Data (BIGDATA)*, 2533–2542.
- 832 Boucheron, L. E., Al-Ghraibah, A., & McAteer, R. T. (2015). PREDICTION of
 833 SOLAR FLARE SIZE and TIME-TO-FLARE USING SUPPORT VECTOR
 834 MACHINE REGRESSION. *The Astrophysical Journal*, 812(1), 51.
- 835 Bruno, A., Christian, E. R., de Nolfo, G. A., Richardson, I. G., & Ryan, J. M.
 836 (2019, March). Spectral Analysis of the September 2017 Solar Energetic
 837 Particle Events. *Space Weather*, 17(3), 419-437. doi: 10.1029/2018SW002085
- 838 Cane, H. V., & Richardson, I. G. (2003). Interplanetary coronal mass ejections in
 839 the near-earth solar wind during 1996-2002. *Journal of Geophysical Research:*
 840 *Space Physics*, 108. doi: 10.1029/2002JA009817
- 841 Chertok, I. M., Belov, A. V., & Abunin, A. A. (2018, October). Solar Erup-

- 842 tions, Forbush Decreases, and Geomagnetic Disturbances From Out-
 843 standing Active Region 12673. *Space Weather*, 16(10), 1549-1560. doi:
 844 10.1029/2018SW001899
- 845 Cohen, C. M. S., Mason, G. M., Mewaldt, R. A., & Wiedenbeck, M. E. (2014,
 846 September). The Longitudinal Dependence of Heavy-ion Composition in the
 847 2013 April 11 Solar Energetic Particle Event. *Atrophys. J.*, 793(1), 35. doi:
 848 10.1088/0004-637X/793/1/35
- 849 Colak, T., & Qahwaji, R. (2009). Automated solar activity prediction: A hybrid
 850 computer platform using machine learning and solar imaging for automated
 851 prediction of solar flares. *Space Weather*, 7(6), 1–12.
- 852 Ding, L., Jiang, Y., Zhao, L., & Li, G. (2013). The “Twin-CME” Scenario and Large
 853 Solar Energetic Particle Events in Solar Cycle 23. *The Astrophysical Journal*,
 854 763(1), 30.
- 855 Ding, Z., Li, G., Hu, J.-X., & Fu, S. (2020, September). Modeling the 2017 Septem-
 856 ber 10 solar energetic particle event using the iPATH model. *Research in As-
 857 tronomy and Astrophysics*, 20(9), 145. doi: 10.1088/1674-4527/20/9/145
- 858 Engell, A. J., Falconer, D. A., Schuh, M., Loomis, J., & Bissett, D. (2017).
 859 SPRINTS: A Framework for Solar-Driven Event Forecasting and Research.
 860 *Space Weather*, 15(10), 1321–1346.
- 861 Falconer, D. A., Moore, R. L., Barghouty, A. F., & Khazanov, I. (2014). MAG4 ver-
 862 sus alternative techniques for forecasting active region flare productivity. *Space
 863 Weather*, 12, 306–317.
- 864 Fulara, A., Chandra, R., Chen, P. F., Zhelyazkov, I., Srivastava, A. K., & Uddin, W.
 865 (2019, May). Kinematics and Energetics of the EUV Waves on 11 April 2013.
 866 *Solar Physics*, 294(5), 56. doi: 10.1007/s11207-019-1445-3
- 867 Garcia, H. A. (2004). Forecasting methods for occurrence and magnitude of proton
 868 storms with solar soft X rays. *Space Weather*, 2(6), n/a–n/a.
- 869 García-Rigo, A., Núñez, M., Qahwaji, R., Ashamari, O., Jiggins, P., Pérez, G., ...
 870 Hilgers, A. (2016). Prediction and warning system of SEP events and solar
 871 flares for risk estimation in space launch operations. *Journal of Space Weather
 872 and Space Climate*, 6, A28.
- 873 Georgoulis, M. K. (2008). Magnetic complexity in eruptive solar active regions and
 874 associated eruption parameters. *Geophysical Research Letters*, 35(6), 5–9.

- 875 Gibson, S. E., & Low, B. C. (1998). A Time-dependent Three-dimensional Magne-
 876 tohydrodynamic Model of the Coronal Mass Ejection. *The Astrophysical Jour-*
 877 *nal*, 493(1), 460–473.
- 878 Gil, A., Modzelewska, R., Moskwa, S., Siluszyk, A., Siluszyk, M., Wawrzynczak,
 879 A., ... Tomasik, L. (2020, October). The Solar Event of 14 - 15 July
 880 2012 and Its Geoeffectiveness. *Solar Physics*, 295(10), 135. doi: 10.1007/
 881 s11207-020-01703-2
- 882 Gombosi, T. I., Chen, Y., Glocer, A., Huang, Z., Jia, X., Liemohn, M. W., ... Zou,
 883 S. (2021). What Sustained Multi-Disciplinary Research Can Achieve: The
 884 Space Weather Modeling Framework. *Journal of Space Weather and Space*
 885 *Climate*, 11.
- 886 Gombosi, T. I., van der Holst, B., Manchester, W. B., & Sokolov, I. V. (2018,
 887 July). Extended MHD modeling of the steady solar corona and the solar wind.
 888 *LRSP*, 15(1), 4.
- 889 Hu, J., Li, G., Ao, X., Zank, G. P., & Verkhoglyadova, O. (2017, Nov). Modeling
 890 Particle Acceleration and Transport at a 2-D CME-Driven Shock. *Journal of*
 891 *Geophysical Research (Space Physics)*, 122(11), 10,938-10,963. doi: 10.1002/
 892 2017JA024077
- 893 Huang, X., Wang, H., Xu, L., Liu, J., Li, R., & Dai, X. (2018). Deep Learning Based
 894 Solar Flare Forecasting Model. I. Results for Line-of-sight Magnetograms. *The*
 895 *Astrophysical Journal*, 856(1), 7.
- 896 Huang, X., Wang, H. N., & Li, L. P. (2012). Ensemble prediction model of solar pro-
 897 ton events associated with solar flares and coronal mass ejections. *Research in*
 898 *Astronomy and Astrophysics*, 12(3), 313–321.
- 899 Huang, Z., Tóth, G., Sachdeva, N., Zhao, L., van der Holst, B., Sokolov, I., ...
 900 Gombosi, T. I. (2023, 4). Modeling the solar wind during different phases
 901 of the last solar cycle. *The Astrophysical Journal Letters*, 946, L47. doi:
 902 10.3847/2041-8213/acc5ef
- 903 Inceoglu, F., Jeppesen, J. H., Kongstad, P., Marcano, N. J. H., Jacobsen, R. H., &
 904 Karoff, C. (2018). Using Machine Learning Methods to Forecast if Solar Flares
 905 Will Be Associated with CMEs and SEPs. *The Astrophysical Journal*, 861(2),
 906 128.
- 907 James, A. W., Green, L. M., van Driel-Gesztelyi, L., & Valori, G. (2020, December).

- 908 A new trigger mechanism for coronal mass ejections. The role of confined flares
 909 and photospheric motions in the formation of hot flux ropes. *AA*, 644, A137.
 910 doi: 10.1051/0004-6361/202038781
- 911 Jin, M., Manchester, W. B., van der Holst, B., Sokolov, I., Toth, G., Mullinix, R. E.,
 912 ... Gombosi, T. I. (2017, January). Data-constrained coronal mass ejections
 913 in a global magnetohydrodynamics model. *The Astrophysical Journal*, 834(2),
 914 173.
- 915 Jin, M., Manchester, W. B., van der Holst, B., Sokolov, I., Tóth, G., Vourli-
 916 das, A., ... Gombosi, T. I. (2017). Chromosphere to 1 au simulation of
 917 the 2011 march 7th event: A comprehensive study of coronal mass ejection
 918 propagation. *The Astrophysical Journal*, 834, 172. Retrieved from
 919 <http://stacks.iop.org/0004-637X/834/i=2/a=172?key=crossref>
 920 .86207496aab2cddb8e5a3abf86182cf1 doi: 10.3847/1538-4357/834/2/172
- 921 Jin, M., Schrijver, C. J., Cheung, M. C. M., DeRosa, M. L., Nitta, N. V., & Ti-
 922 tle, A. M. (2016, 3). A numerical study of long-range magnetic impacts
 923 during coronal mass ejections. *The Astrophysical Journal*, 820, 16. doi:
 924 10.3847/0004-637x/820/1/16
- 925 Jing, J., Inoue, S., Lee, J., Li, Q., Nita, G. M., Xu, Y., ... Wang, H. (2021, Decem-
 926 ber). Understanding the Initiation of the M2.4 Flare on 2017 July 14. *Astro-*
 927 *phys. J.*, 922(2), 108. doi: 10.3847/1538-4357/ac26c7
- 928 Jivani, A., Sachdeva, N., Huang, Z., Chen, Y., van der Holst, B., Manchester, W.,
 929 ... Toth, G. (2023, 1). Global sensitivity analysis and uncertainty quantifica-
 930 tion for background solar wind using the alfvén wave solar atmosphere model.
 931 *Space Weather*, 21. doi: 10.1029/2022SW003262
- 932 Joshi, B., Kushwaha, U., Veronig, A. M., Dhara, S. K., Shanmugaraju, A., & Moon,
 933 Y.-J. (2017, January). Formation and Eruption of a Flux Rope from the
 934 Sigmoid Active Region NOAA 11719 and Associated M6.5 Flare: A Multi-
 935 wavelength Study. *Atrophys. J.*, 834(1), 42. doi: 10.3847/1538-4357/834/1/
 936 42
- 937 Kasapis, S., Zhao, L., Chen, Y., Wang, X., Bobra, M., & Gombosi, T. I. I. (2022,
 938 feb). Interpretable machine learning to forecast SEP events for Solar Cycle 23.
 939 *Space Weather*, 20(2), e02842. doi: 10.1029/2021SW002842
- 940 Kataoka, R., Ebisuzaki, T., Kusano, K., Shiota, D., Inoue, S., Yamamoto, T. T., &

- 941 Tokumaru, M. (2009). Three-dimensional mhd modeling of the solar wind
 942 structures associated with 13 december 2006 coronal mass ejection. *Journal of*
 943 *Geophysical Research: Space Physics*, 114. doi: 10.1029/2009JA014167
- 944 Kouloumvakos, A., Patsourakos, S., Nindos, A., Vourlidas, A., Anastasiadis, A.,
 945 Hillaris, A., & Sandberg, I. (2016, April). Multi-viewpoint Observations
 946 of a Widely distributed Solar Energetic Particle Event: The Role of EUV
 947 Waves and White-light Shock Signatures. *Atrophys. J.*, 821(1), 31. doi:
 948 10.3847/0004-637X/821/1/31
- 949 Kozarev, K., Nedal, M., Miteva, R., Dechev, M., & Zucca, P. (2022, Febru-
 950 ary). A Multi-Event Study of Early-Stage SEP Acceleration by CME-
 951 Driven Shocks—Sun to 1 AU. *Frontiers in Astronomy and Space Sciences*,
 952 9. Retrieved from [https://www.frontiersin.org/article/10.3389/](https://www.frontiersin.org/article/10.3389/fspas.2022.801429)
 953 [fspas.2022.801429](https://www.frontiersin.org/article/10.3389/fspas.2022.801429) doi: 10.3389/fspas.2022.801429
- 954 Kozarev, K. A., Davey, A., Kendrick, A., Hammer, M., & Keith, C. (2017, Novem-
 955 ber). The Coronal Analysis of SHocks and Waves (CASHew) framework.
 956 *JSWSC*, 7, A32. doi: 10.1051/swsc/2017028
- 957 Krymsky, G. F. (1977). A regular mechanism for the acceleration of charged parti-
 958 cles on the front of a shock wave. *Soviet Physics-Doklady*, 234, 1306.
- 959 Kühl, P., Banjac, S., Dresing, N., Gómez-Herrero, R., Heber, B., Klassen, A., &
 960 Terasa, C. (2015, April). Proton intensity spectra during the solar energetic
 961 particle events of May 17, 2012 and January 6, 2014. *Astronomy & Astrophys.*,
 962 576, A120. doi: 10.1051/0004-6361/201424874
- 963 Lario, D., Ho, G. C., Roelof, E. C., Anderson, B. J., & Korth, H. (2013, January).
 964 Intense solar near-relativistic electron events at 0.3 AU. *Journal of Geophysical*
 965 *Research (Space Physics)*, 118(1), 63-73. doi: 10.1002/jgra.50106
- 966 Lario, D., Raouafi, N. E., Kwon, R.-Y., Zhang, J., Gómez-Herrero, R., Dresing, N.,
 967 & Riley, P. (2014). The solar energetic particle event on 2013 april 11: an in-
 968 vestigation of its solar origin and longitudinal spread. *The Astrophysical Jour-*
 969 *nal*, 797, 8. Retrieved from <http://arxiv.org/abs/1410.5490v5>
 970 <http://arxiv.org/abs/1410.5490v5>
 971 [dx.doi.org/10.1088/0004-637X/797/1/8](http://arxiv.org/abs/1410.5490v5)
 972 <http://arxiv.org/abs/1410.5490v5>
 973 [doi: 10.1088/0004-637X/797/1/8](http://arxiv.org/abs/1410.5490v5)
- 974 Laurenza, M., Cliver, E. W., Hewitt, J., Storini, M., Ling, A. G., Balch, C. C., &

- 974 Kaiser, M. L. (2009). A technique for short-term warning of solar energetic
 975 particle events based on flare location, flare size, and evidence of particle es-
 976 cape. *Space Weather*, 7(4), 1–18.
- 977 Li, C., Firoz, K., Sun, L., & Miroshnichenko, L. (2013, June). Electron and Proton
 978 Acceleration during the First Ground Level Enhancement Event of Solar Cycle
 979 24. *Atrophys. J.*, 770(1), 34. doi: 10.1088/0004-637X/770/1/34
- 980 Li, G., Jin, M., Ding, Z., Bruno, A., de Nolfo, G., Randol, B., ... Lario, D. (2021).
 981 Modeling the 2012 May 17 Solar Energetic Particle Event Using the AW-
 982 SoM and iPATH Models. *The Astrophysical Journal*, 919(2), 146. doi:
 983 10.3847/1538-4357/ac0db9
- 984 Li, G., Moore, R., Mewaldt, R. A., Zhao, L., & Labrador, A. W. (2012). A Twin-
 985 CME Scenario for Ground Level Enhancement Events. *Space Science Reviews*,
 986 171, 141–160.
- 987 Linker, J. A., Caplan, R. M., Schwadron, N., Gorby, M., Downs, C., Torok, T., ...
 988 Wijaya, J. (2019, May). Coupled MHD-Focused Transport Simulations for
 989 Modeling Solar Particle Events. *Journal of Physics: Conference Series*, 1225,
 990 012007. doi: 10.1088/1742-6596/1225/1/012007
- 991 Lugaz, N., Iv, W. B. M., Roussev, I. I., Tóth, G., & Gombosi, T. I. (2007). *Numer-*
 992 *ical investigation of the homologous coronal mass ejection events from active*
 993 *region 9236* (Vol. 659).
- 994 Lugaz, N., Manchester, W. B., & Gombosi, T. I. (2005). Numerial simulation of the
 995 interaction of two coronal mass ejections from Sun to Earth. *The Astrophysical*
 996 *Journal*, 634, 651–662.
- 997 Luhmann, J., Ledvina, S., Krauss-Varban, D., Odstrcil, D., & Riley, P. (2007, jan).
 998 A heliospheric simulation-based approach to sep source and transport model-
 999 ing. *Adv. Space Res.*, 40(3), 295–303. doi: 10.1016/j.asr.2007.03.089
- 1000 Manchester, W., Gombosi, T., De Zeeuw, D., Sokolov, I., Roussev, I., Powell, K.,
 1001 ... Zurbuchen, T. (2005, April). Coronal mass ejection shock and sheath
 1002 structures relevant to particle acceleration. *The Astrophysical Journal*, 622,
 1003 1225–1239.
- 1004 Manchester, W., Gombosi, T. I., De Zeeuw, D. L., Sokolov, I. V., Roussev, I. I.,
 1005 Powell, K. G., ... Zurbuchen, T. H. (2005, April). Coronal mass ejection
 1006 shock and sheath structures relevant to particle acceleration. *The Astrophysical*

- 1007 *Journal*, 622, 1225–1239.
- 1008 Manchester, W., van der Holst, B., Toth, G., & Gombosi, T. (2012, SEP 1). The
 1009 coupled evolution of electrons and ions in coronal mass ejection-driven shocks.
 1010 *The Astrophysical Journal*, 756(1).
- 1011 Manchester, W., Vourlidas, A., Toth, G., Lugaz, N., Roussev, I. I., Sokolov, I. V.,
 1012 ... Opher, M. (2008, September). Three-dimensional MHD simulation of the
 1013 2003 October 28 coronal mass ejection: Comparison with LASCO coronagraph
 1014 observations. *The Astrophysical Journal*, 684(2), 1448–1460.
- 1015 Manchester, W. B., Gombosi, T. I., Roussev, I., Ridley, A., Zeeuw, D. L. D.,
 1016 Sokolov, I. V., ... Tóth, G. (2004). Modeling a space weather event from
 1017 the sun to the earth: Cme generation and interplanetary propagation. *Journal*
 1018 *of Geophysical Research: Space Physics*, 109. doi: 10.1029/2003JA010150
- 1019 Manchester, W. B., Gombosi, T. I., Roussev, I., Zeeuw, D. L. D., Sokolov, I. V.,
 1020 Powell, K. G., ... Opher, M. (2004). Three-dimensional mhd simulation of a
 1021 flux rope driven cme. *Journal of Geophysical Research: Space Physics*, 109.
 1022 doi: 10.1029/2002JA009672
- 1023 Manchester, W. B., Kozyra, J. U., Lepri, S. T., & Lavraud, B. (2014). Simulation of
 1024 magnetic cloud erosion during propagation. *Journal of Geophysical Research:*
 1025 *Space Physics*, 119, 5449–5464. doi: 10.1002/2014JA019882
- 1026 Manchester, W. B., Ridley, A. J., Gombosi, T. I., & DeZeeuw, D. L. (2006). Mod-
 1027 eling the sun-to-earth propagation of a very fast cme. *Advances in Space Re-*
 1028 *search*, 38, 253–262. doi: 10.1016/j.asr.2005.09.044
- 1029 Manchester, W. B., & van der Holst, B. (2017, September). The Interaction of Coro-
 1030 nal Mass Ejections with Alfvénic Turbulence. In *Journal of physics conference*
 1031 *series* (Vol. 900, p. 012015).
- 1032 Manchester, W. B., van der Holst, B., & Lavraud, B. (2014, mar). Flux rope evo-
 1033 lution in interplanetary coronal mass ejections: the 13 May 2005 event. *Plasma*
 1034 *Physics and Controlled Fusion*, 56(6), 1–11.
- 1035 Manchester, W. B., van der Holst, B., Toth, G., & Gombosi, T. I. (2012, SEP 1).
 1036 The coupled evolution of electrons and ions in coronal mass ejection-driven
 1037 shocks. *The Astrophysical Journal*, 756(1).
- 1038 Manchester, W. B., Vourlidas, A., Toth, G., Lugaz, N., Roussev, I. I., Sokolov, I. V.,
 1039 ... Opher, M. (2008, September). Three-dimensional MHD simulation of the

- 2003 October 28 coronal mass ejection: Comparison with LASCO coronagraph
observations. *The Astrophysical Journal*, *684*(2), 1448–1460.
- Marsh, M. S., Dalla, S., Dierckxsens, M., Laitinen, T., & Crosby, N. B. (2015).
SPARX: A modeling system for Solar Energetic Particle Radiation Space
Weather forecasting. *Space Weather*, *13*(6), 386–394.
- Mays, M. L., Thompson, B. J., Jian, L. K., Colaninno, R. C., Odstreil, D., Möstl,
C., ... Zheng, Y. (2015, October). Propagation of the 7 January 2014
CME and Resulting Geomagnetic Non-event. *Atrophys. J.*, *812*(2), 145. doi:
10.1088/0004-637X/812/2/145
- Mishev, A. L., Kocharov, L. G., & Usoskin, I. G. (2014, February). Analysis of the
ground level enhancement on 17 May 2012 using data from the global neutron
monitor network. *Journal of Geophysical Research (Space Physics)*, *119*(2),
670-679. doi: 10.1002/2013JA019253
- Möstl, C., Rollett, T., Frahm, R. A., Liu, Y. D., Long, D. M., Colaninno, R. C., ...
Vršnak, B. (2015, May). Strong coronal channelling and interplanetary evolu-
tion of a solar storm up to Earth and Mars. *Nature Communications*, *6*, 7135.
doi: 10.1038/ncomms8135
- Nunez, M. (2011). Predicting solar energetic proton events ($E > 10$ MeV). *Space
Weather*, *9*(7).
- Núñez, M. (2015). Real-time prediction of the occurrence and intensity of the first
hours of >100 MeV solar energetic proton events. *Space Weather*, *13*(11), 807–
819.
- Papaioannou, A., Anastasiadis, A., Sandberg, I., Georgoulis, M. K., Tsiropoula, G.,
Tziotziou, K., ... Hilgers, A. (2015). A Novel Forecasting System for So-
lar Particle Events and Flares (FORSPEF). *Journal of Physics: Conference
Series*, *632*(1).
- Park, E., Moon, Y.-J., Shin, S., Yi, K., Lim, D., Lee, H., & Shin, G. (2018). Ap-
plication of the Deep Convolutional Neural Network to the Forecast of Solar
Flare Occurrence Using Full-disk Solar Magnetograms. *The Astrophysical
Journal*, *869*(2), 91.
- Patsourakos, S., Georgoulis, M. K., Vourlidas, A., Nindos, A., Sarris, T., Anagnos-
topoulos, G., ... Vlahos, L. (2016, January). The Major Geoeffective Solar
Eruptions of 2012 March 7: Comprehensive Sun-to-Earth Analysis. *APJ*,

- 1073 817(1), 14. doi: 10.3847/0004-637X/817/1/14
- 1074 Posner, A. (2007). Up to 1-hour forecasting of radiation hazards from solar energetic
1075 ion events with relativistic electrons. *Space Weather*, 5(5), 1–28.
- 1076 Qin, G., Zhang, M., & Dwyer, J. R. (2006). Effect of adiabatic cooling on the fitted
1077 parallel mean free path of solar energetic particles. *Journal of Geophysical Re-*
1078 *search*, 111(A8), A08101.
- 1079 Reames, D. V. (2013). The two sources of solar energetic particles. *Space Science*
1080 *Reviews*, 175, 53–92.
- 1081 Richardson, I. G., & Cane, H. V. (2010). Near-earth interplanetary coronal mass
1082 ejections during solar cycle 23 (1996 - 2009): Catalog and summary of proper-
1083 ties. *Solar Physics*, 264, 189–237. doi: 10.1007/s11207-010-9568-6
- 1084 Richardson, I. G., Mays, M. L., & Thompson, B. J. (2018). Prediction of Solar Ener-
1085 getic Particle Event Peak Proton Intensity Using a Simple Algorithm Based on
1086 CME Speed and Direction and Observations of Associated Solar Phenomena.
1087 *Space Weather*, 16(11), 1862–1881.
- 1088 Richardson, I. G., von Rosenvinge, T. T., Cane, H. V., Christian, E. R., Cohen,
1089 C. M. S., Labrador, a. W., . . . Stone, E. C. (2014, apr). > 25 MeV Proton
1090 Events Observed by the High Energy Telescopes on the STEREO A and B
1091 Spacecraft and/or at Earth During the First Seven Years of the STEREO
1092 Mission. *Sol. Phys.*, 289, 3059.
- 1093 Roussev, I. I. (2008). Eruptive events in the solar atmosphere: new insights from
1094 theory and 3-D numerical modelling. *Journal of Contemporary Physics*, 49(4),
1095 237–254.
- 1096 Roussev, I. I., Sokolov, I. V., Forbes, T. G., Gombosi, T. I., Lee, M. A., & Sakai,
1097 J. I. (2004). A numerical model of a coronal mass ejection: Shock develop-
1098 ment with implications for the acceleration of GeV protons. *The Astrophysical*
1099 *Journal Letter*, 605, L73–L76.
- 1100 Sachdeva, N., van der Holst, B., Manchester, W. B., Tóth, G., Chen, Y., Lloveras,
1101 D. G., . . . Henney, C. J. (2019, dec). Validation of the Alfvén wave solar at-
1102 mosphere model (AWSOM) with observations from the low corona to 1 au. *The*
1103 *Astrophysical Journal*, 887(1), 83.
- 1104 Schwadron, N. A., Townsend, L., Kozarev, K., Dayeh, M. A., Cucinotta, F., De-
1105 sai, M., . . . Squier, R. K. (2010, January). Earth-Moon-Mars Radiation

- Environment Module framework. *Space Weather*, 8(10), S00E02. doi:
10.1029/2009SW000523
- Scolini, C., Rodriguez, L., Mierla, M., Pomoell, J., & Poedts, S. (2019, June).
Observation-based modelling of magnetised coronal mass ejections with EU-
HFORIA. *Astronomy & Astrophys.*, 626, A122. doi: 10.1051/0004-6361/
201935053
- Shen, C., Li, G., Kong, X., Hu, J., Sun, X. D., Ding, L., ... Xia, L. (2013, 2).
Compound twin coronal mass ejections in the 2012 may 17 gle event. *The As-
trophysical Journal*, 763, 114. Retrieved from [http://stacks.iop.org/0004-
637X/763/i=2/a=114?key=crossref.78f34351bc8e5988061c2cae2a8b599c](http://stacks.iop.org/0004-637X/763/i=2/a=114?key=crossref.78f34351bc8e5988061c2cae2a8b599c)
doi: 10.1088/0004-637X/763/2/114
- Shen, C., Xu, M., Wang, Y., Chi, Y., & Luo, B. (2018, July). Why the Shock-ICME
Complex Structure Is Important: Learning from the Early 2017 September
CMEs. *APJ*, 861(1), 28. doi: 10.3847/1538-4357/aac204
- Shiota, D., & Kataoka, R. (2016, 2). Magnetohydrodynamic simulation of in-
terplanetary propagation of multiple coronal mass ejections with inter-
nal magnetic flux rope (susanoo-cme). *Space Weather*, 14, 56-75. doi:
10.1002/2015SW001308
- Smart, D. F., & Shea, M. A. (1976). PPS76 - A Computerized "Event Mode" Solar
Proton Forecasting Technique. *Journal of Atmospheric and Solar-Terrestrial
Physics*, 406.
- Smart, D. F., & Shea, M. A. (1989). PPS-87: A new event oriented solar proton pre-
diction model. *Advances in Space Research*, 9(10), 281–284.
- Smart, D. F., & Shea, M. A. (1992). Modeling the time intensity profile of solar flare
generated particle fluxes in the inner heliosphere. *Advances in Space Research*,
12(2), 303–312.
- Sokolov, I. V., Roussev, I. I., Gombosi, T. I., Lee, M. A., Kóta, J., Forbes, T. G.,
... Sakai, J. I. (2004). A New Field Line Advection Model for Solar Particle
Acceleration. *The Astrophysical Journal*, 616(2), L171–L174.
- Sokolov, I. V., van der Holst, B., Manchester, W. B., Ozturk, D. C. S., Szente, J.,
Taktakishvili, A., ... Gombosi, T. I. (2021). Threaded-field-lines model for the
low solar corona powered by the Alfvén wave turbulence. *The Astrophysical
Journal*, 908(1), 172–183.

- 1139 Sokolov, I. V., van der Holst, B., Oran, R., Downs, C., Roussev, I. I., Jin, M., ...
 1140 Gombosi, T. I. (2013). Magnetohydrodynamic waves and coronal heating:
 1141 Unifying empirical and MHD turbulence models. *The Astrophysical Journal*,
 1142 *764*, 23.
- 1143 Sokolov, I. V., Zhao, L., & Gombosi, T. I. (2022). Stream-aligned magnetohydrody-
 1144 namics for solar wind simulations. *Astrophys. J.*, *926*(1), 102. doi: 10.3847/
 1145 1538-4357/ac400f
- 1146 Strauss, R. D., & Fichtner, H. (2015, March). On Aspects Pertaining to the Perpen-
 1147 dicular Diffusion of Solar Energetic Particles. *APJ*, *801*(1), 29. doi: 10.1088/
 1148 0004-637X/801/1/29
- 1149 Tenishev, V., Shou, Y., Borovikov, D., Lee, Y., Fougere, N., Michael, A., & Combi,
 1150 M. R. (2021, feb). Application of the Monte Carlo method in modeling
 1151 dusty gas, dust in plasma, and energetic ions in planetary, magnetospheric,
 1152 and heliospheric environments. *Journal of Geophysical Research*, *126*(2),
 1153 e2020JA028242.
- 1154 Thakur, N., Gopalswamy, N., Xie, H., Mäkelä, P., Yashiro, S., Akiyama, S., &
 1155 Davila, J. M. (2014, July). Ground Level Enhancement in the 2014 Jan-
 1156 uary 6 Solar Energetic Particle Event. *Atrophys. J. Lett.*, *790*(1), L13. doi:
 1157 10.1088/2041-8205/790/1/L13
- 1158 Tiwari, S. K., Falconer, D. A., Moore, R. L., Venkatakrishnan, P., Winebarger,
 1159 A. R., & Khazanov, I. G. (2015, 7). Near-sun speed of cmes and the magnetic
 1160 nonpotentiality of their source active regions. *Geophysical Research Letters*,
 1161 *42*, 5702-5710. doi: 10.1002/2015GL064865
- 1162 van der Holst, B., Jacobs, C., & Poedts, S. (2007, nov). Simulation of a breakout
 1163 coronal mass ejection in the solar wind. *The Astrophysical Journal*, *671*(1),
 1164 L77–L80.
- 1165 van der Holst, B., Manchester, W., IV, Sokolov, I. V., Toth, G., Gombosi, T. I.,
 1166 DeZeeuw, D., & Cohen, O. (2009, March). Breakout coronal mass ejection
 1167 or streamer blowout: The bugle effect. *The Astrophysical Journal*, *693*(2),
 1168 1178–1187.
- 1169 van der Holst, B., Sokolov, I. V., Meng, X., Jin, M., Manchester, W. B., Toth, G.,
 1170 & Gombosi, T. I. (2014, jan). Alfvén Wave Solar Model (AWSOM): Coronal
 1171 Heating. *Astrophys. J.*, *782*(2), 81. doi: 10.1088/0004-637X/782/2/81

- Vemareddy, P., & Mishra, W. (2015, November). A Full Study on the Sun-Earth Connection of an Earth-directed CME Magnetic Flux Rope. *Atrophys. J.*, 814(1), 59. doi: 10.1088/0004-637X/814/1/59
- Wang, Y., & Qin, G. (2015). Simulations of the Spatial and Temporal Invariance in the Spectra of Gradual Solar Energetic Particle Events. *The Astrophysical Journal*, 806(2), 252.
- Whitman, K., Egeland, R., Richardson, I. G., Allison, C., Quinn, P., Barzilla, J., ... Valtonen, E. (2022). Review of Solar Energetic Particle models. *Adv. Space Res.*, 000, 000–000. (<https://doi.org/10.1016/j.asr.2022.08.006>) doi: xxx
- Wijsen, N., Aran, A., Sanahuja, B., Pomoell, J., & Poedts, S. (2020, February). The effect of drifts on the decay phase of SEP events. *Astronomy & Astrophysics*, 634, A82. doi: 10.1051/0004-6361/201937026
- Wijsen, N., Aran, A., Scolini, C., Lario, D., Afanasiev, A., Vainio, R., ... Poedts, S. (2022, March). Observation-based modelling of the energetic storm particle event of 14 July 2012. *Astronomy & Astrophysics*, 659, A187. doi: 10.1051/0004-6361/202142698
- Young, M. A., Schwadron, N. A., Gorby, M., Linker, J., Caplan, R. M., Downs, C., ... Cohen, C. M. (2020). Energetic proton propagation and acceleration simulated for the bastille day event of july 14, 2000. *The Astrophysical Journal*, 909, 160. Retrieved from <http://dx.doi.org/10.3847/1538-4357/abdf5f> doi: 10.3847/1538-4357/abdf5f
- Zhang, M., & Zhao, L. (2017). Precipitation and release of solar energetic particles from the solar coronal magnetic field. *The Astrophysical Journal*, 846(2), 107.
- Zhao, L., & Li, G. (2014). Particle acceleration at a pair of parallel shocks near the Sun. *Journal of Geophysical Research: Space Physics*, 119, 6106–6119.
- Zhao, L., Li, G., Zhang, M., Wang, L., Moradi, A., & Effenberger, F. (2019). Statistical analysis of interplanetary magnetic field path lengths from solar energetic electron events observed by wind. *The Astrophysical Journal*, 878, 107. Retrieved from <http://dx.doi.org/10.3847/1538-4357/ab2041> doi: 10.3847/1538-4357/ab2041
- Zhao, L., Zhang, M., & Rassoul, H. K. (2016). Double Power Laws in the Event-Integrated Solar Energetic Particle Spectrum. *The Astrophysical Journal*, 821(1), 62.

- 1205 Zhao, L., Zhang, M., & Rassoul, H. K. (2017). The Effects of Interplanetary Trans-
1206 port in the Event-intergrated Solar Energetic Particle Spectra. *The Astrophysi-
1207 cal Journal*, 836(1), 1–10.
- 1208 Zhu, B., Liu, Y. D., Kwon, R.-Y., Jin, M., Lee, L. C., & Xu, X. (2021, November).
1209 Shock Properties and Associated Characteristics of Solar Energetic Particles
1210 in the 2017 September 10 Ground-level Enhancement Event. *Atrophys. J.*,
1211 921(1), 26. doi: 10.3847/1538-4357/ac106b